# Time-Resolved Wall Shear Rate Mapping using High-Frame-Ultrasound Imaging

by

Chung Kit Ho

A thesis

presented to the University of Waterloo

in fulfillment of the

thesis requirement for the degree of

Master of Applied Science

in

Electrical and Computer Engineering

Waterloo, Ontario, Canada, 2018

# Author’s declaration

I hereby declare that I am the sole author of this thesis. This is a true copy of the thesis, including any required final revisions, as accepted by my examiners.

I understand that my thesis may be made electronically available to the public.

# Abstract

Arterial wall shear rate is known to be strongly associated with plaque formation and stroke risk. As a non-invasive, point-of-care imaging modality, ultrasound has been applied to perform wall shear rate (WSR) measurements. However, the existing ultrasound-based solutions fall short of providing sufficient diagnostic information in both spatial and temporal dimensions while remaining non-invasive. To date, quantitatively tracking WSR dynamics over multiple vessel wall positions has yet to be demonstrated. In this work, we propose a new non-invasive WSR mapping technique that makes use of high-frame-rate ultrasound principles to dynamically track the spatiotemporal evolution of WSR in an artery segment.

The proposed new WSR mapping method is built on two key principles: high-frame-rate-flow vector estimation and velocity gradient estimation via a two-dimensional spatial derivative. In brief, after high-frame-rate ultrasound data using plane wave excitation, a set of flow vector maps was generated using a multi-angle vector Doppler estimation. Next, the flow vector maps were regularized using a penalized least-squares method. After that, a Sobel filter was used to derive the spatial velocity gradients of the vector map. Finally, the WSR was computed by finding the tangential components of the velocity gradient tensors at the vessel wall positions.

Two studies were carried out to investigate the performance of the proposed WSR measurement method. First, a Hele-Shaw flow chamber that can generate a linear WSR field was designed and constructed to evaluate the accuracy of the wall shear rate estimation. Second, two carotid bifurcation models (healthy and 50% stenosed) were built to demonstrate the ability of the framework to quantify and visualize spatiotemporal WSR patterns in complex flow dynamics. Results from the first study indicate that the proposed estimation algorithm can provide consistent WSR estimates. Findings from

the second study suggest that our proposed framework is capable of profiling space-time varying WSR dynamics, which could provide new insights in atherosclerosis diagnostics.

# Acknowledgments

Studying my master's degree abroad has been a life-changing experience for me. Immersing myself in a new culture, exploring new places, making new friends from different countries are always fascinating. There are a couple of people who have been supporting me throughout my study. I would like to use this opportunity to express my gratitude to them.

First, I would like to thank my supervisor, Prof. Alfred Yu. Thank you for offering me an opportunity to study at the University of Waterloo. I would not dream of travelling all the way to Canada to research if you did not give me a chance.

I would also like to thank the lab members of LITMUS, especially Billy Yiu, Adrian Chee, and Takuro Ishii. Thank you for sharing your experience and knowledge in research. Working with you was fantastic. Also, exploring Waterloo with such a great group of people was always fun.

Finally, I would like to thank my parents and Stephanie Lam for continuously providing me with spiritual support and encouragement throughout my study. I would not have made it through without you.

# Table of Contents

# List of Figures

**Figures**

# List of Tables

**Tables**

# List of Abbreviations

| Abbreviations | |
|---|---|
| 2-D | Two-dimensional |
| 3-D | Three-dimensional |
| B-mode | Brightness-mode |
| BMF | Blood mimicking fluid |
| CAD | Computer-aided design |
| CCA | Common carotid artery |
| CFD | Computational fluid dynamics |
| CFI | Colour flow imaging |
| DCT | Discrete cosine transform |
| ECA | External carotid artery |
| FIR | Finite impulse response |
| GCV | Generalized cross-validation |
| GPU | Graphical processing unit |
| HRI | High-resolution image |
| ICA | Internal carotid artery |
| IDCT | Inverse discrete cosine transform |
| IIR | Infinite impulse response |
| LSI | Low-resolution image |
| MRI | Magnetic resonance imaging |
| NASCET | North America Symptomatic Carotid Endarterectomy Trial |
| PLA | Polylactic acid |
| PVA | Polyvinyl alcohol |
| RF | Radio frequency |
| RMSE | Root-mean-squared-error |
| ROI | Region of interest |
| Rx | Receive |
| SNR | Signal-to-noise ratio |
| Tx | Transmit |
| WSR | Wall shear rate |
| WSS | Wall shear stress |

# List of Symbols

**Imaging Parameters**

| | |
|---|---|
| $c_0$ | Speed of sound |
| $f_c$ | Centre frequency |
| $f_d$ | Doppler frequency |
| $f_{DAQ}$ | Effective data acquisition rate |
| $t_d$ | Time delay between successive received signals |
| $v_{limit}$ | Maximum detectable velocity without aliasing |
| $\theta_{bf}$ | Beam-flow angle |
| $\lambda$ | Wavelength |
| $\phi$ | Phase of the received RF signal |
| $\varphi_T$ | Transmit angle |
| $\varphi_R$ | Receive angle |
| $\omega$ | Angular frequency |

**Signal and Image Processing Parameters**

| | |
|---|---|
| A | Area |
| $b$ | Block length |
| $f_{cutoff}$ | Normalized cut-off frequency of a clutter filter |
| $\mathbf{G}_{ij}$ | Gradient map in $i^{th}$ direction derived from the $j^{th}$-direction velocity map |
| $\mathbf{I}$ | Identity matrix |
| $J_i(.)$ | Bessel function of the first kind and order $i$ |
| $K_{i,p}$ | Sobel kernel for $i^{th}$ direction gradient computation of size $p$ |
| $p$ | Penalty term in cost function |
| $\mathbf{Q}$ | Rotation matrix |
| r | Radial displacement |
| $(r_p,c_p)$ | Pixel coordinate |
| $(\bar{r}_p,\bar{c}_p)$ | Pixel coordinate of a centroid |
| $R_y(1)$ | Autocorrelation function evaluated at a lag of one sample |
| $s$ | Smoothing parameter |
| $\tilde{v}$ | Normalized velocity |
| $v_{clutter}$ | Maximum velocity affected by clutter filtering |
| $\mathbf{V}_i$ | Velocity vector map in $i^{th}$ direction |
| $\beta$ | Angle between the tangential direction at a wall position and the horizontal axis |
| $\varepsilon$ | Gaussian noise |

**Flow Parameters and Physical Dimensions**

| | |
|---|---|
| $h$ | Gap height of the flow channel |
| $L$ | Total length of the flow channel |
| $w$ | Width of the flow channel |
| $w_0$ | Entrance width of the flow channel |
| $P$ | Pressure |
| Q | Flow rate |
| R | Radius of a vessel lumen |
| $S_{ij}$ | Shear rate tensor |
| $v_{max}$ | Maximum flow velocity |
| $\boldsymbol{v}$ | Flow velocity vector |
| $\alpha$ | Womersley number |
| $\dot{\gamma}_w$ | Wall shear rate |
| $\mu$ | Dynamic viscosity |
| $\rho$ | Density |
| $\tau_w$ | Wall shear stress |

# CHAPTER 1

# Introduction to Arterial Wall Shear Rate

## 1.1 Chapter Overview

Arterial wall shear stress (WSS), and its surrogate wall shear rate (WSR) have been extensively studied due to its relevance to cardiovascular diseases. This chapter introduces the role of WSR in human arteries. It begins with a discussion of the causes of WSR-related diseases, including atherosclerosis and stroke. The subsequent section describes how WSR alters the progression of these diseases. The highlights of existing WSR estimation modalities and their features are then considered. The final section outlines the motivation and hypothesis of this research study, as well as the research objectives.

## 1.2 Clinical Background

### 1.2.1 Atherosclerosis and Stroke

Atherosclerosis is the dominant cause of cardiovascular disease which is the leading cause of death globally. There are approximately 17.7 million death cases due to cardiovascular diseases in 2015, representing 31% of global mortality (World Health Organization, 2017). The most significant risk factors include high cholesterol and low-density lipoprotein, low level of high-density lipoprotein in the blood, hypertension, smoking, diabetes, obesity, lack of physical activity, aging (Nayer & Ortega, 2014; Owen, Lindsay, Choudhury, & Fayad, 2011; Weber & Noels, 2011). Atherosclerosis is an inflammatory disease characterized by the development of plaques that cause a reduction in the lumen of the arteries. (illustrated in Fig. 1.1). Plaque is composed of fat, calcium, cholesterol, and other substances that are present in blood circulation (Weaver, 2013). It could be unstable and prone to rupture because of the altered blood flow pattern (Ku, Giddens, Zarins, & Glaygoy, 1985). It leads

to an increased risk of ischemic stroke which causes loss of brain function due to the inadequate blood supply to the brain (Martin, Zaman, Hacker, Mendelow, & Birchall, 2009; Shields, 2010). In Canada, stroke is the thirding leading cause of death among all diseases. Every year, there are approximately 62,000 new stroke cases, causing more than 13,000 deaths (Heart and Stroke Foundation of Canada, 2016).

Plaque represents the hallmark lesion of atherosclerosis. The severity of stenosis has been assessed using the peak systolic velocity at the stenosed site (Gaitini & Soudack, 2005). However, the presence or severity of stenotic plaques does not necessarily imply the occurrence of stroke. In fact, 90% of the stenosis cases may be of low stroke risk, and they can be treated using drug therapy and dietary treatment (Spence, 2013). Hence, it is important to distinguish between high-risk and low-risk stenosis cases so that the patients with low stroke risk can be spared from highly invasive surgical treatments such as endarterectomy (removal of the plaque material) and stenting (placement of a mesh tube within the blood vessel) (Spence & Naylor, 2016). As such, it is of clinical interest to develop a fast and non-invasive diagnostic technology to identify the potential risk for stroke, without solely relying on the vascular morphological changes.

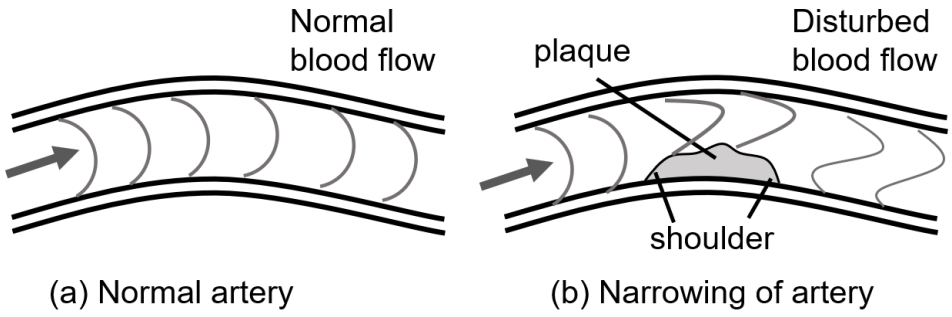


Fig. 1.1 (a) A normal artery with normal blood flow. (b) A diseased artery with plaque buildup. The blood flow is disturbed due to the narrowing of the artery. Rupture-prone shoulder regions of the plaque are marked.

## 1.2.2 Arterial Wall Shear Rate and Wall Shear Stress

Monitoring of the hemodynamics in carotid arteries, especially at the bifurcation region, is known to be of value to the prognosis of stroke (Donnan, Fisher, Macleod, & Davis, 2008). Among various hemodynamic parameters, WSS is considered to be of high clinical relevance to stroke diagnostics because it is strongly related to atherosclerotic plaque formation (Dhawan et al. 2010), as well as the plaque progression and possible rupture (Makris, Nicolaides, Xu, & Geroulakos, 2010).

WSS is defined as the shear force per unit area exerted on the arterial wall due to the viscous flowing blood. Specifically, a low average WSS level stimulates the vascular endothelial cells to enhance the oxidation of lipids and their accumulation on the inner lining (Malek, Alper, & Izumo, 1999; Kinlay, Libby, & Ganz, 2001). As a result, plaque development is favoured, and the rate of atherosclerosis progression is increased (Gibson et al., 1993). In contrast, a high WSS level implies that the blood is exerting a considerable amount of shearing force to the plaque, especially at the shoulder area (as pointed out in Fig. 1.1). This high shearing force may increase the risk of plaque rupture at the latter stages of atherosclerosis (Tuenter et al., 2016). Therefore, routinely monitoring the WSS level may provide useful clinical information for early atherosclerosis diagnosis. In practice, WSR can be measured to gauge the corresponding WSS because of their proportional relationship, which is subsequently discussed in Section 2.5. Up to date, a few non-invasive modalities have demonstrated their possibilities in measuring WSR. The following subsection will discuss their key measurement principles and major limitations.

## 1.2.3 Existing Non-invasive Modalities for Wall Shear Rate Estimation

***Computational Fluid Dynamic Simulation***

Computational Fluid Dynamics (CFD) simulation is one of the widely used techniques to compute various fluid dynamic parameters, including flow velocities and WSR. It has been reported that a high-resolution reconstruction of hemodynamics based on carotid bifurcation models can be

obtained using CFD (Birchall, Zaman, Hacker, Davies, & Mendelow, 2006). However, the computational time for CFD simulation is rather long, typically on the order of hours. Also, it requires a 3-D image volume scan, such as computed tomography, for a detailed vascular geometry (Jin et al., 2004) to construct a model for simulations. Also, acquisition of patient-specific boundary conditions (e.g., inlet and outlet flow profile, local blood pressure) remains clinically challenging (Morris et al., 2015). Hence, CFD simulation may not be the best option for clinical application since the resources for computation are usually somewhat limited.

***Magnetic Resonance Imaging***

Another WSR estimation method is using Magnetic Resonance Imaging (MRI). It has been demonstrated that Phase-contrast MRI can be used to estimate the flow velocities of the blood (Oshinski, Curtin, & Loth, 2006; Carvalho, Nielsen, & Nayak, 2010). The WSR can then be derived from the flow velocity vectors. However, the temporal resolution of MRI is limited because the measurements are typically obtained over 25 to 30s (Reneman, Arts, & Hoeks, 2006; Yim, Demarco, & Castro, 2005). The MRI scan has to be carried out simultaneously with Electrocardiogram gating to yield an adequate temporal resolution. However, it significantly prolongs the scan time (about an hour) for flow velocities estimation. Moreover, the size of MRI scanners is rather big, and it requires a Radio Frequency (RF) shield magnet room. Therefore, this imaging modality may not be suitable for bedside WSR assessments or routine clinical WSR measurements.

***Ultrasound-based Approach***

Ultrasound imaging is known as a point-of-care diagnostic tool (Moore & Copel, 2011) that has been widely used by clinicians to aid in diagnosis because of its real-time scanning capability, compact size, and high accessibility. It is considered as one of the safest imaging modalities because it does not involve any ionizing radiation. Its scanning time is much shorter than that in MRI (Murphy et al., 2017). A few ultrasound-based WSR estimation schemes have been proposed, including spectral Doppler (Hoskins, 2010), color flow imaging (Struijk et al., 2005; Tsou, Liu, Barakat, &

Insana, 2008), and echo particle image velocimetry (Kim, Hertzberg, Lanning, & Shandas, 2004; Leow & Tang, 2018). Nevertheless, these existing imaging methods have limited spatial dimension (single site WSR measurement) or temporal resolution while remaining non-invasive. The fundamental principles and limitations of these methods will be reviewed in Chapter 2.

## 1.3 Outline of Thesis Study

### 1.3.1 Motivation and Hypothesis

Recent technological development in ultrasound imaging has significantly improved its data acquisition rate without compromising the field-of-view. Based on the use of broad-field ultrasound transmission schemes (Bercoff et al., 2011; Diagle & Kaczdowski, 2009; Hasegawa & Kanai, 2008; Xu, Choi, Comess, & Kim, 2010), time-resolved images of complex flow dynamics can be acquired at a high temporal resolution. Also, it has been demonstrated that flow velocities can be robustly estimated at every pixel position from those high-frame-rate images (Yiu, Lai, & Yu, 2014). With these foundations, we hypothesize that the WSR dynamics can be tracked at high temporal resolution (sub-millisecond range), and a spatiotemporal WSR mapping can be achieved.

### 1.3.2 Research Objectives

The overall goal of this project is to develop a high-frame-rate WSR imaging tool that can quantify the WSR in complex flow dynamics. Specifically, this work will seek to accomplish the following two research objectives:

1) Develop a WSR estimation algorithm and examine its accuracy under well-characterized flow geometries and known flow conditions.

2) Evaluate the practical effectiveness of the proposed WSR estimation method by conducting *in vitro* studies using anthropomorphic carotid flow phantoms.

Well-characterized flow geometries often give a stable, or slowly changing flow profile which is useful for calibration purposes. However, the WSR measurement in these geometries may not provide insights on WSR estimation in human vasculature, which are usually curved and branched. Therefore, we propose to use anatomically realistic flow phantoms to examine the practical effectiveness of the WSR estimation. Carotid artery models are chosen in particular because of two reasons. First, the WSR in carotid arteries is known to be associated with stroke-related events, such as plaque formation and rupture (Gnasso et al., 1997; Malek et al., 1999). Due to this physiological relevance, WSR measurement in the carotid artery models can provide us insights on how the proposed WSR estimation method can be used in assessing stroke risk. Second, the geometric features of the carotid artery models allow us to test the ability of the proposed WSR estimation in tracking WSR patterns with spatiotemporal variations. Also, the flow dynamics in these geometries have been characterized by others using optical particle imaging velocimetry (Kefayati & Poepping, 2013; Poepping, Rankin, & Holdsworth, 2010) and contrast-enhanced ultrasound imaging (Leow & Tang, 2018). This information provides us with an established reference for comparison with the WSR measured using the proposed method.

# CHAPTER 2

# Wall Shear Rate Estimation using Ultrasound Imaging

## 2.1 Chapter Overview

Ultrasound imaging, also known as medical ultrasound, has been widely used in non-invasive vascular diagnosis (Evans, 2010). High-frame-rate technique is one of the breakthroughs that enable many new potential clinical applications of ultrasound (Tanter & Fink, 2014). Although there is a considerable amount of technological innovations in the ultrasound research, many of the principles used in conventional method still apply. Therefore, Section 2.2 discusses the fundamental principles in ultrasound imaging. Next, the concepts of high-frame-rate ultrasound technique are described in Section 2.3. Being an essential component in WSR measurement, the theory of the flow velocity vector estimation will be presented in Section 2.4. Section 2.5 begins with the discussion of WSR and WSR from the physics point of view, followed by a review of existing ultrasound-based WSR measurement techniques. The last section introduces some performance investigation strategies for ultrasound flow imaging, including the choice of materials and model designs.

## 2.2 Background of Ultrasound Imaging

### 2.2.1 Physical Principles

In general, ultrasound imaging is done by sending sound wave with high frequencies (typically 1-20 MHz) into body tissues and receiving the echo using a piezoelectric transducer. The speed of sound ($c_0$) in soft tissue is approximately 1540 m/s. The relationship of the frequency, the speed of sound, and its wavelength can be described by the wave equation:

$$c_0 = f_c \lambda \tag{2-1}$$

where $f_c$ is the centre frequency of the transmitted ultrasound wave, and $\lambda$ is the wavelength. As the waves propagate through body tissues, part of the ultrasound waves is reflected due to three types of reflection: specular reflection, backscattering, and Rayleigh scattering. Rayleigh scattering takes place when the scatterers are small relative to the ultrasound wavelength. A common example of Rayleigh scattering is the scattering generated by red blood cells. These echoes are then returned to the transducer. The detected echoes are converted into electrical signals, which become the RF signal for processing. The remaining ultrasound waves continue to penetrate into the tissues and repeat the same process until the all the ultrasound waves are attenuated within the tissue.

### 2.2.2 Doppler Equation and Velocity

The modern velocity estimation scheme is based on a pulsed wave Doppler approach. As depicted in Fig. 2.1a, consider a single scatter moving in the imaging medium with velocity $\boldsymbol{v}$. Let the pulse repetition frequency (PRF) of the ultrasound pulses transmission be $f_{\mathrm{PRF}}$. The received signals are illustrated in Fig. 2.1b. The terms "slow time" and "fast time" are referred to as the dimension between subsequent firings and along the ultrasound beam respectively. The time delay between successive received signals ($t_d$) is given by the following expression:

$$t_{\mathrm{d}} = \frac{2\Delta z}{c_0} = \frac{2|\boldsymbol{v}| \cos \theta_{\mathrm{bf}}}{c_0 f_{\mathrm{PRF}}} \tag{2-2}$$

where $\Delta z$ is the axial displacement of the scatterer, and $\theta_{\mathrm{bf}}$ is the beam-flow angle (angle between the beam-axis and the moving direction of the scatterer, i.e., the flow direction).

The phase shift of the fast-time signals is then given by $\Delta\phi = 2\pi f_c t_d$. Note that (i) the fast-time phase shift is identical to the slow-time one, and (ii) the center frequency of the slow-time signal (as shown in 2.1c) is $f_d = \Delta\phi \cdot f_{\mathrm{PRF}}/2\pi$. Hence,

$$f_{\mathrm{d}} = \frac{\Delta\phi}{\Delta t} = f_{\mathrm{c}} t_{\mathrm{d}} f_{\mathrm{PRF}} \tag{2-3}$$

Substituting (2-2) into (2-3), we can obtain the following form:

$$f_{\mathrm{d}} = \frac{2|\boldsymbol{v}| \cos\theta_{\mathrm{bf}} f_{\mathrm{c}}}{c_0} \tag{2-4}$$

(2-4) is known as the Doppler equation, which relates the Doppler frequency and the scatterer velocity. Although (2-4) is equivalent to the Doppler equation for finding the change in wavelength (i.e., Doppler shift), there is no wavelength or frequency change throughout the imaging process. Instead, the phase shift is the actual quantity being measured in most velocity estimation algorithms. The set of RF signals obtained from the consecutive firings is often called an ensemble, and the number of firings for one ensemble is called the ensemble size.

According to the Nyquist theorem, to avoid aliasing in the RF signal sampling, $t_d$ must be no greater than half period of the transmission frequency $f_c$. With this requirement, the maximum detectable velocity ($v_{\mathrm{limit}}$) is given by:

$$v_{\mathrm{limit}} = \pm \frac{c_0 f_{\mathrm{PRF}}}{4 f_{\mathrm{c}} \cos\theta_{\mathrm{bf}}} \tag{2-5}$$

In practice, the phase shift $\Delta\phi$ is often estimated using an autocorrelation technique such as 1-D autocorrelation method by Kasai and Namekawa (1985). For a Doppler data vector $\mathbf{y} = [y(0), y(1),\ldots, y(N_D\text{-}1)]^{\mathrm{T}}$, the autocorrelation estimator is given by:

$$f_{\mathrm{d}} = \frac{f_{\mathrm{PRF}}}{2\pi} \arg\{R_{\mathrm{y}}(1)\} \tag{2-6}$$

where $R_y(1)$ is the autocorrelation function evaluated at a lag of one sample and is given by:

$$R_y(1) = \frac{1}{N_D} \sum_{n=1}^{N_D-1} y(n) y^*(n-1) \tag{2-7}$$

where $N_D$ is the data length.

As such, this estimation technique is often called lag-one-autocorrelation phase algorithm. As can be seen from (2-6) and (2-7), the phase estimation is, in fact, a mean Doppler frequency estimation.

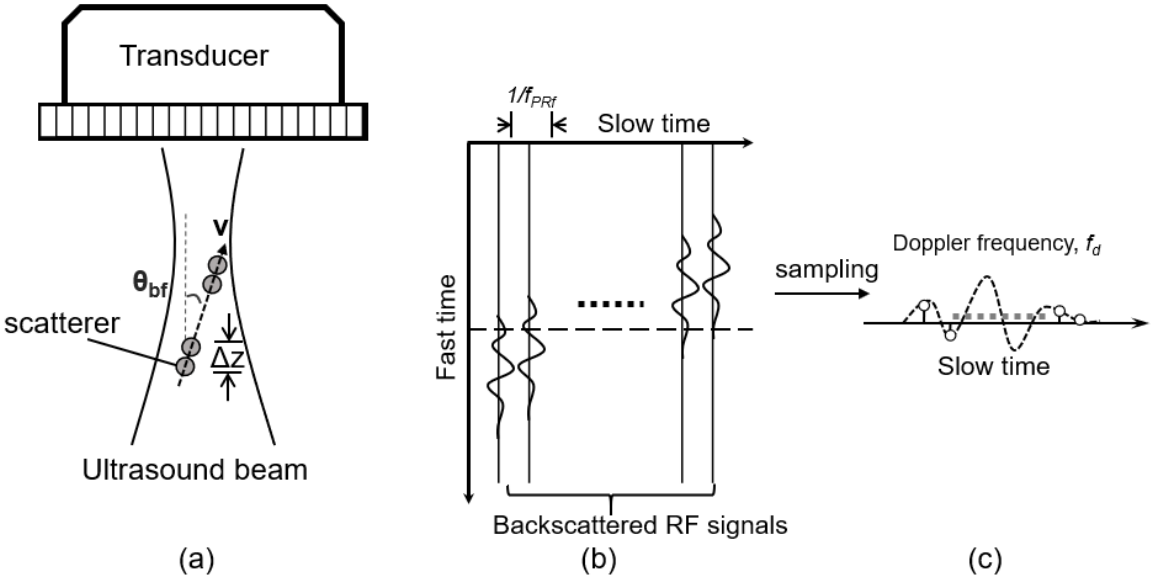


Fig. 2.1. Illustration of velocity estimation scheme using pulsed ultrasound method. (a) The movement of a single scatterer through the sample volume. (b) Received RF signals from the backscattering of the scatterer at each firing. (c) Reconstructed slow-time waveform by sampling RF signals in (b), with the centre frequency equal to the Doppler frequency $f_d$.

## 2.3. High-frame-rate Data Acquisition Technique

Being able to monitor the hemodynamics within a single cardiac cycle is one of the important features of ultrasound-based imaging modalities. However, the data acquisition rate of conventional ultrasound imaging is often limited. In conventional systems, firing focused beams can insonify only a narrow region of the medium (as illustrated in Fig. 2.2a). A single image is then formed using the echoes from multiple transmissions (typically of the order of magnitude $10^1$). Hence, the number of transmissions is equal to the number of scan lines to be formed. The frame rate is then limited to about 30 to 40 Hz without sacrificing the spatial dimension (Montaldo, Tanter, Bercoff, Benech, &

Fink, 2009). A higher data acquisition rate can provide the necessary temporal resolution to resolve more complex blood flow dynamics in various phases of the cardiac cycle. In addition, it provides a larger amount of data for velocity estimation. Since the velocity estimation variance is inversely proportional to the number of observation (i.e., ensemble size), it enables more precise velocity estimates. Moreover, the high-frame-rate technique allows a wider dynamic range of the flow as the maximum detectable velocity is limited by the acquisition rate $f_{PRF}$, as described in (2-5).

### 2.3.1. Plane Wave Transmission Scheme

Plane wave transmission is a novel data acquisition technique to achieve high-frame-rate imaging (Mo et al., 2003; Sandarin, Manneville, & Fink, 2001). Instead of firing focused beamlines, plane waves are emitted to the entire region of interest (ROI), as illustrated in Fig. 2.2. Hence, the frame rate is no longer coupled to the number of scan lines and the ROI which are the major factors that limit the frame rate in the conventional method. Typically, the plane wave transmission technique can increase the acquisition rate of the ultrasound scan by hundred-fold as compared to the one using conventional method. While it is possible to construct one image from a single plane wave transmission (Fig. 2.2b), a few so-called low-resolution images (LRIs) formed from successive planes waves pulse-echo at different steering angles (angle between the beam-axis and the direction of depth) are usually combined to obtain a high-resolution image (HRI) (see Fig. 2.2c). For $M$ Tx angles, the effective data acquisition rate ($f_{DAQ}$) is given by $f_{PRF}/M$. The benefits of using this approach are twofold. First, the flow direction can be determined by solving the Doppler equation at different steering angles. It overcomes the limitation of ambiguous beam-flow angles in conventional CFI method. Second, it has been proved that the signal-to-noise ratio (SNR) can be improved by compounding a few images. The reason is that since the plane wave is unfocused, the signal power is lower than that acquired using the conventional method. Combining the LSIs can reduce the random noise in the images, thereby increasing the SNR.

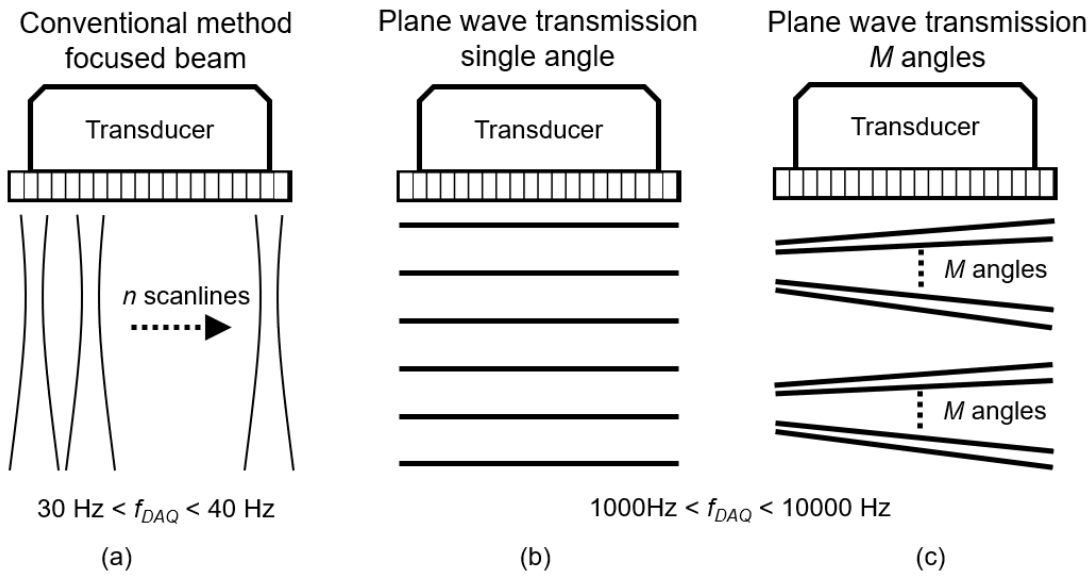


Fig. 2.2. (a) Conventional scanline-based imaging approach which requires combing *n* scanlines to form one image. High-frame-rate data acquisition technique using plane wave transmission scheme with (b) single steering angle, and (c) multiple *M* angles.

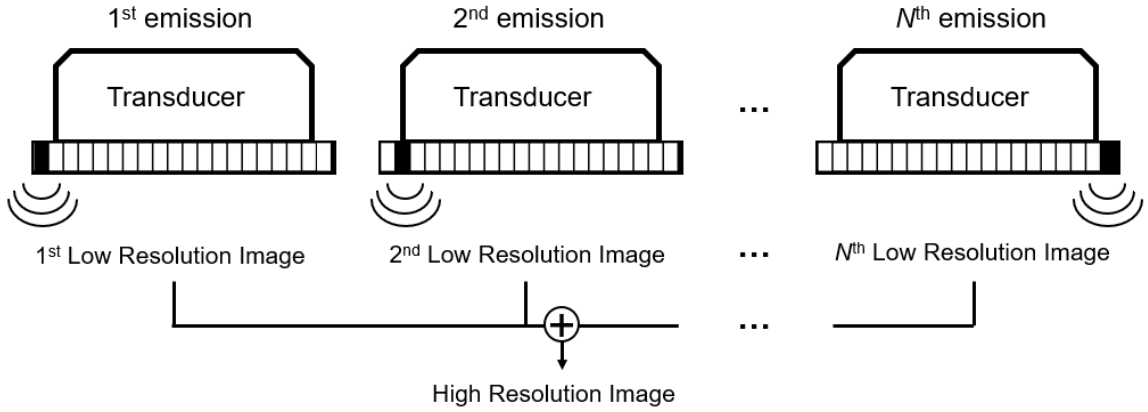


Fig. 2.3. High-frame-rate data acquisition technique using synthetic aperture imaging. Spherical waves are emitted using a single transducer element. *N* LSIs are combined to form a single HRI.

## 2.3.2 Synthetic Aperture Imaging

Synthetic aperture imaging is another new high-frame-rate technique in ultrasound imaging (Flaherty, Erikson, & Lund, 1970; Burckhardt, Grandchamp, & Hoffmann, 1974). A few transducer elements are used to transmit a spherical wave insonifies the entire ROI. The echo from each emission

is received using all elements. It yields a single LRI and multiple LRIs formed are compounded to generate a synthetic image, also known as HRI (as illustrated in Fig. 2.3). Therefore, the acquisition rate $f_{DAQ}$ is equal to $f_{PRF}/N$. The state-of-the-art synthetic aperture imaging yields similar frame rate to that of plane wave imaging (i.e., approximately 1 to 10 kHz). Similar to the plane wave transmission scheme, this approach also allows the determination of flow angles. Various literature has demonstrated the possibility of using synthetic aperture approach for velocity estimation (Jensen, Nikolov, Gammelmark, & Pedersen, 2006). However, a fundamental problem in synthetic aperture imaging requires a large amount of calculations (Montaldo et al., 2009; Jensen, Nikolov, Yu, & Garcia, 2016). Graphical processing unit (GPU) technique has been introduced to reduce the data processing time (Tanter & Fink, 2014). Also, a dual-stage approach called synthetic aperture sequential beamforming method has been suggested to reduce the data amount and processing demand (Kortbek, Jensen, & Gammelmark, 2013).

# 2.4. Generating Velocity Vector Map using Multi-angle Doppler

## 2.4.1 Concepts of Multi-angle Doppler

As seen in the Doppler equation (2-4), the beam-flow angle $\theta_{bf}$ is required to solve for the Doppler shift, hence the velocity estimate. However, θ is often unknown in practice. It results in an uncertainty in the velocity estimation. To address this issue, Peronneau, Bournat, Bugnon, Barbet, & Xhaard (1974) and Hansen, Cross, & Light (1974) have developed multi-angle Doppler (sometimes referred to as cross-beam Doppler) to derive the flow vector information. As reviewed by Jensen et al. (2016), this approach can be realized by first generalizing the (2-4) into arbitrary transmit angle $\varphi_T$ and receive angle $\varphi_R$,

$$f_d = \frac{|\boldsymbol{v}| \cos(\varphi_T - \theta_{bf}) + |\boldsymbol{v}| \cos(\varphi_R - \theta_{bf})}{c_0} f_c \qquad (2\text{-}8)$$

Next, using trigonometry identities and decomposing the velocity vector into its lateral (x-direction) and axial (z-direction) components (where $\boldsymbol{v} = v_x\hat{\mathbf{i}} + v_z\hat{\mathbf{j}} = |\boldsymbol{v}|\sin\theta\hat{\mathbf{i}} + |\boldsymbol{v}|\cos\theta\hat{\mathbf{j}}$), (2-4) becomes:

$$v_z(\cos\varphi_{\mathrm{T}} + \cos\varphi_{\mathrm{R}}) + v_x(\sin\varphi_{\mathrm{T}} + \sin\varphi_{\mathrm{R}}) = \frac{c_0 f_{\mathrm{d}}}{f_{\mathrm{c}}} \qquad (2\text{-}9)$$

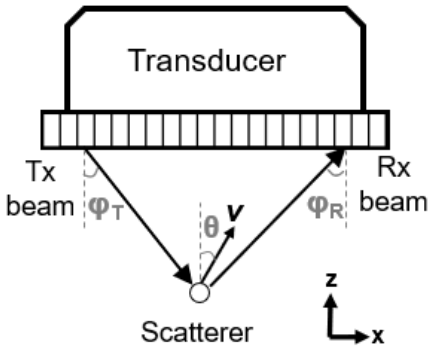


Fig. 2.4. Illustration of multiple-angle Doppler acquisition with transmit angle $\varphi_T$ and receive angle $\varphi_R$.

Note that the transmit angle $\varphi_T$ and receive angle $\varphi_R$ are user-defined parameters, so two Doppler frequencies $f_d$ need to be measured at different Tx-Rx angle pairs to solve for $v_x$ and $v_z$. The application of such dual-angle approach in blood flow velocity measurement has been demonstrated in some studies (Hansen et al., 1974; Wang & Yao, 1982; Dunmire, Beach, Labs, Plett, & Strandness, 2000).

## 2.4.2. Multi-angle Doppler with High-Frame-Rate Acquisition

While two Tx-Rx pairs are necessary to solve (2-9), it has been demonstrated the flow vectors can be robustly estimated by solving an overdetermined system of linear equations with multiple angle pairs (Yiu et al., 2014; Yiu & Yu, 2016). For *M* Tx-angles and *N* Rx-angles, (2-9) can be expressed in matrix form:

$$\begin{bmatrix} cos\varphi_{T_1} + cos\varphi_{R_1} & sin\varphi_{T_1} + sin\varphi_{R_1} \\ \vdots & \vdots \\ cos\varphi_{T_M} + cos\varphi_{R_N} & sin\varphi_{T_M} + sin\varphi_{R_N} \end{bmatrix} \begin{bmatrix} v_z \\ v_x \end{bmatrix} = \begin{bmatrix} u_{11} \\ \vdots \\ u_{MN} \end{bmatrix} \quad \text{(2-10a)}$$

or

$$\mathbf{Av} = \mathbf{u} \quad \text{(2-10b)}$$

where $u_{MN} = cf_{d,MN}/f_c$.

Hence, the flow vector **v** in (2-10a) can be determined by taking the pseudo-inverse of **A** with **u**, i.e., $\mathbf{v} = (\mathbf{A}^T\mathbf{A})^{-1}\mathbf{A}^T\mathbf{u}$. Such operation is also referred to as a least-squares fitting solution (Moon & Stirling, 2000). The advantage of using the multi-angle approach is that it increases the total number of Doppler frequency estimates (i.e., $f_d$) available for vector flow estimation. It can reduce the estimation variance from the lag-one autocorrelation estimation. The velocity estimates are computed based on least mean-squared error, hence providing more consistent flow vector estimates.

# 2.5. Deriving Wall Shear Rate from Flow Velocities

## 2.5.1 Definition of Wall Shear Rate and Wall Shear Stress

WSS is defined as the tangential force per unit area that is exerted by the flowing fluid on the surface of a conduit tube (e.g., blood vessel). In medium and large arteries, such as carotid arteries, blood can be assumed to be a Newtonian fluid which has a constant dynamic viscosity (Reneman et al., 2006). In general, shear stress (denoted by $\tau$) is a second rank symmetric tensor and can be expressed in:

$$\tau_{ij} = \mu\left(\frac{\partial v_i}{\partial x_j} + \frac{\partial v_j}{\partial x_i}\right) \quad (i \neq j) \quad \text{(2-11)}$$

With the Newtonian fluid assumption, WSS ($\tau_w$) can be calculated by multiplying the dynamic viscosity of blood ($\mu$) by the WSR ($\dot{\gamma}_w$), as described in (2-12). In a 2-D flow, (2-12) can be simplified into (2-13). Theoretically, if the velocity flow profile in the blood vessel is determined,

the WSR can be calculated by taking the derivative of the tangential velocity components in the wall normal direction, as depicted in Fig. 2.5. Note that shear stress is usually measured in Pa ($N/m^2$) and shear rate is measured in reciprocal seconds ($s^{-1}$). The relationship between WSS and WSR and then be described as:

$$\tau_w = \mu \cdot \dot{\gamma}_w \tag{2-12}$$

$$\tau_w = \mu \frac{\partial v_{x'}}{\partial z'}|_{z'=0} \tag{2-13}$$

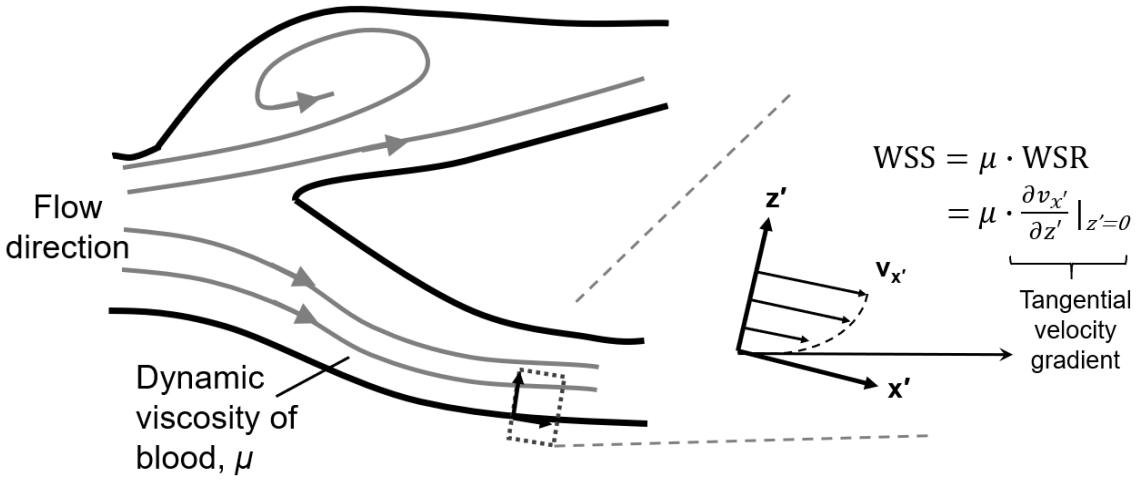


Fig. 2.5. Conceptual illustration of WSS and WSR measurement in a carotid bifurcation. WSR is defined by the tangential velocity gradient at the vessel wall. WSS is the product of the dynamic viscosity of blood $\mu$ and WSR.

## 2.5.2 Existing Ultrasound-based Techniques for Wall Shear Rate Estimation

***Colour Flow Imaging***

Colour flow imaging (CFI) outputs images of the variation of the flow velocities over an imaging view on a colour-coded scale. The colour velocity map is overlaid upon the gray-scale B-mode image (refer to Fig. 2.6a), as shown in Fig.2.6b. The WSR can then be computed from the

obtained velocity profiles. A few WSR estimation algorithms have been reported based on this technique (Struijk et al., 2005; Tsou et al., 2008). However, this imaging mode is known to possess methodical flaws (Evans, 2010). In a colour flow image, the beam-flow angle is user-defined and fixed. However, the blood flow inside arteries is rarely unidirectional as the vasculature is not in straight-tube form. Therefore, the variations in the beam-flow angle within an imaging view have a significant impact on the accuracy of the flow velocities estimation, thereby limiting the accuracy of the WSR estimates. Also, the frame rate provided by CFI is often inadequate to provide accurate mapping of the actual flow conditions (Evans, 2010).

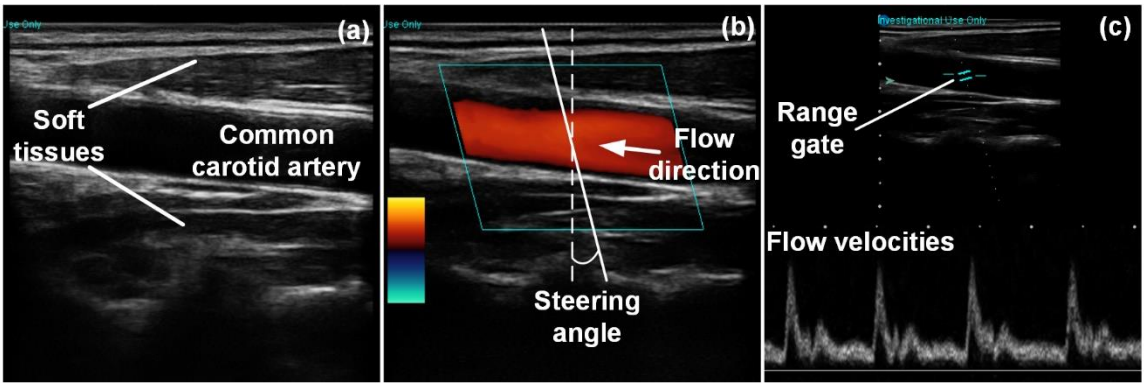


Fig. 2.6. (a) A B-mode image of a segment of a common carotid artery. (b) A colour flow image. The steering angle is indicated. The colour represents the magnitude and direction of the flow (red indicates that the flow is moving towards the transducer). (c) A Doppler Spectrogram displaying the flow velocity profile measured within the range gate.

***Spectral Doppler***

Spectral Doppler is a technique that allows us to estimate the flow velocity distribution at a single point, or within a small window (Cobbold, 2007), as shown in Fig. 2.6c. A range gate with adjustable size is placed at the selected position on a B-mode image to measure the Doppler frequencies at that position. The Doppler frequencies are then converted into the flow velocities using the Doppler equation (2-4). Placing the gate across the vessel lumen, the velocity gradient, hence the WSR can be derived (Hoskins, 2010). Although spectral Doppler method provides a sufficient temporal resolution (2-10 ms), the spatial dimension of this approach is very limited because the gate

size is typically smaller than a few millimetres. In other words, the WSR at only a single or a few positions can be estimated at a time. However, in carotid bifurcation arteries, the WSR patterns are often spatially varying. The limited spatial dimension in the provided information may cause difficulties in interpreting the measurement results.

***Echo particle image velocimetry***

Ultrasound flow imaging can be enhanced by introducing contrast agents, such as fluorocarbon-based microbubbles (Mehta, Lee, Taha, Avgerinos, & Chaer, 2017). It provides a stronger scattering strength for flow measurement. Echo particle image velocimetry has been proposed for WSR estimation (Kim et al., 2004; Leow & Tang, 2018). The velocity vectors estimation is based on tracking the trajectories of the particles, i.e., microbubbles, in the vessel lumen by performing cross-correlation operations between frames (Leow et al., 2015; Zhang et al., 2010). The WSR can then be derived from the vector maps. Although the use of contrast agents can improve the SNR, the backscattered signals from the scatterer can be easily lost due to the out-of-plane motion of the particles (Hansen et al., 2009). More importantly, the non-invasiveness of ultrasound imaging will be compromised. It is because the microbubbles need to be injected into the human body through intravenous administration; moreover, the clinical safety of using microbubbles for routine clinical applications remains controversial (Stride & Coussios, 2010). It has been reported that the use of contrast agents is linked to temporary back pain and hypotension (Herzog, 2008).

## 2.5.3 Challenges in Wall Shear Rate Estimation Algorithm

***Presence of tissue clutter***

It may seem straightforward to estimate wall shear rate from a velocity vector map; however, the measurement of the velocities close to the vessel wall has remained a challenge in ultrasound imaging (Cobbold, 2007). Within the flow region, there are in general three types of signals received by the transducer: blood signal, tissue clutter, and white noise. In velocity estimation, the blood signal from the blood scatterers (i.e., red blood cells) is the desired signal. Meanwhile, the surrounding tissue

(e.g., vessel wall) also gives a very high amplitude signal. These clutter signals are typically 40 to 60 dB stronger than the blood signals (Cobbold, 2007). The clutter signals are produced from relatively stationary or slowing moving tissues, so the frequency spectrum of them is lower than that of the blood (as shown in Fig. 2.7). If the clutter signals are not removed, the measured frequency spectrum will be significantly lowered because of its high amplitude nature.

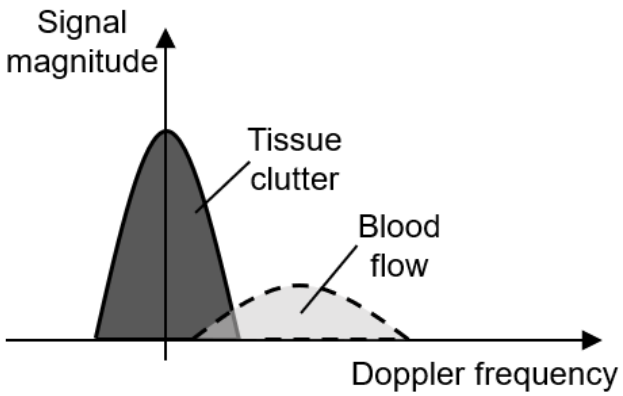


Fig. 2.7. Frequency spectrum of blood signal and tissue clutter.

Commonly, clutter rejection is done by implementing high-pass filter using either finite impulse response (FIR) filter or infinite impulse response (IIR) filter. However, because the blood flow velocity approaches zero at the vessel wall, the lower end of the frequency spectrum of the blood signal typically overlap the clutter signal spectrum. Therefore, the suppression of tissue clutter would introduce bias in the near wall velocity estimates, thereby altering the velocity profile.

***Mathematical models for velocity profile reconstruction***

To reconstruct the velocity profile, the most convenient way to estimate WSR would be using a mathematical model. The Hagen-Poiseuille model has been extensively studied and implemented in clinical scanners (Carallo, Lucca, Ciamei, Tucci, & Franceschi, 2006; Cho, Kim, Kim, & Heo, 2016). In this model, the vessel is assumed to be a straight, axisymmetric pipe with radius R. The simplest assumption on the flow profile would be a fully developed, steady flow with following velocity profile:

$$v(r) = v_{\max}\left(1 - \left|\frac{r}{R}\right|^{n}\right) \tag{2-14}$$

where $n = 2$ for parabolic flow, $r$ is the radial distance, $v_{max}$ refers to the maximum flow velocity.

Hence, the WSR $\dot{\gamma}_w$ becomes:

$$\dot{\gamma}_{\mathrm{w}} = \frac{2v_{\max}}{R} \tag{2-15a}$$

(2-15a) can also be expressed in terms of flow rate $Q$:

$$\dot{\gamma}_{\mathrm{w}} = \frac{4Q}{\pi R^3} \tag{2-15b}$$

In (2-15a), only the maximum flow velocity (the centerline velocity) has to be measured. Therefore, those earlier efforts rely on the measured maximum velocity to estimate the WSR. The rationale is that higher velocity flow is less affected by the clutter, thus providing a relatively accurate estimate. However, the steady flow assumption is invalid because blood flow is pulsatile and the flow can never be fully developed with the compliant vessel walls. This oversimplified flow condition would inevitably limit the accuracy of the estimation, especially in carotid bifurcations with stenosis (Kefayati, Milner, Holdsworth, & Poepping, 2014). It has been reported that using a parabolic profile to estimate the WSS may cause 20-50% error in average (Mynard, Wasserman, & Steinman, 2013).

As a remedy, Womersley flow has been proposed to model the pulsatile blood flow (Evans and McDicken 2000; Womersley, 1955). The pressure gradient is represented using Fourier series. Hence, the pulsatile flow is decomposed into the sum of a steady flow component and $N$ oscillatory components. The velocity profile obtained from the Womersley flow is given as follows:

$$v(r,t) = \frac{P'_0}{4\mu}(R^2 - r^2) + Re\left\{\sum_{n=1}^{N}\frac{iP'_n}{\rho n\omega}\left[1 - \frac{J_0(\Lambda_n\frac{r}{R})}{J_0(\Lambda_n)}\right]e^{in\omega t}\right\} \tag{2-16}$$

where $P'$ is the pressure gradient, $\rho$ is the fluid density, $\omega$ is the angular frequency of the oscillatory component, $J_0(\cdot)$ is the Bessel function of the first kind and order zero, and $\Lambda_n = \alpha n^{1/2} i^{3/2}$. $\alpha$ is the

Womersley number representing the ratio of inertial forces to viscous forces in the flow. Taking the derivative of (2-16) gives the wall shear rate as:

$$\dot{\gamma}_{\mathrm{w}} = Re\left\{\sum_{n=1}^{N} \frac{P'_n R}{\mu \Lambda_n}\left[\frac{J_1(\Lambda_n)}{J_0(\Lambda_n)}\right] e^{in\omega t}\right\} \tag{2-17}$$

where $J_1(\cdot)$ is the Bessel function of the first kind and order one.

Although the Womersley model takes the oscillatory part into account, the estimation accuracy still suffers from the idealistic assumption of a straight pipe condition. The flow velocity profiles in branching vessels and straight vessels are very different (Brech and Bellhouse, 1973). Moreover, the waveform of blood flow varies in different parts of the circulatory system. It has been reported that the blood flow velocity waveforms are different in carotid, femoral and brachial arteries (Azran et al., 2004). Also, the waveforms will be influenced by postural changes (Azran et al., 2004).

# 2.6. Performance Investigation Tools for Ultrasound Imaging

## 2.6.1 Existing Flow Chamber Design for Evaluation of Ultrasound-based Wall Shear Rate Estimation

To assess the performance of wall shear rate estimation, a flow chamber with well-characterized flow parameters, such as velocity field and flow rate, is necessary. Given a user-defined flow inlet and outlet boundary conditions, we can compare the WSR estimates against the theoretical values. A straight tube model has been widely used for this purpose (Kim et al., 2004, Leow & Tang, 2018). The experimental results are compared to the analytical values calculated using (2-15). Different WSR values can be obtained through varying the input flow rate or changing the lumen diameter (as described in 2-15b). However, the issue is that within the same imaging view, only a single WSS value can be obtained using the straight tube model. To fully assess the sensitivity of the

estimation algorithm, a flow channel that can provide a spatially varying WSR pattern will be beneficial to the performance investigation.

***Hele-Shaw flow chamber with linear wall shear rate field***

A Hele-Shaw flow model is perhaps a better design for this purpose. It is essentially a parallel plate flow chamber with a thin gap. It can generate a linear WSR pattern without changing the dimension or the flow rate. It has been used in studying the endothelial cell responses under the varying magnitudes of wall shear stress (Usami, Chen, Zhao, Chien, & Skalak, 1993; Tsou et al., 2008). For incompressible flow, the governing equations are given by:

$$\boldsymbol{\nabla} \cdot \boldsymbol{v} = 0 \tag{2-18}$$

$$\rho \frac{\partial \boldsymbol{v}}{\partial t} + \rho \boldsymbol{v} \cdot \boldsymbol{\nabla} \boldsymbol{v} = -\boldsymbol{\nabla} P + \mu \nabla^2 u + \rho \boldsymbol{g} \tag{2-19}$$

(2-18) is continuity equation and (2-19) is Navier-Stokes equation. In Hele-Shaw flow, the viscous forces dominate while the inertial forces are negligible. Hence the inertia term $\boldsymbol{v} \cdot \boldsymbol{\nabla} \boldsymbol{v}$ is assumed zero. Given a steady flow and negligible gravitational effect, (2-19) becomes:

$$\begin{aligned} \frac{\partial P}{\partial x} &= \frac{\partial^2 v_x}{\partial^2 z} \\ \frac{\partial P}{\partial y} &= \frac{\partial^2 v_y}{\partial^2 z} \\ \frac{\partial P}{\partial z} &= 0 \end{aligned} \tag{2-20}$$

The coordinate system for this particular derivation is shown in Fig. 2.8.

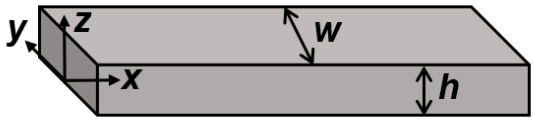


Fig. 2.8. A schematic description of a Hele-Shaw configuration.

Applying no-slip boundary condition, i.e., $\boldsymbol{v}|_{z=0} = \boldsymbol{v}|_{z=h} = 0$, to (2-20), the velocity profile can be written as follows:

$$\boldsymbol{v} = -\frac{1}{2\mu}\,\boldsymbol{\nabla}Pz(h-z) \tag{2-21}$$

Expressing (2-12) in terms of the mean velocity vector $\bar{\mathbf{v}}$,

$$\boldsymbol{v} = -\frac{6}{h^2}\,z(h-z)\bar{\boldsymbol{v}} \tag{2-22}$$

If the gap height is sufficiently small, the flow can be assumed two-dimensional flow, which can be represented by potential flow because of their identical governing equations. A stagnation flow at a right-angled corner is considered to design a flow channel with a linear wall shear rate field. The velocity vectors are given by:

$$\bar{v}_x = 2Cx$$

$$\bar{v}_y = -2Cy \tag{2-23}$$

where $C = -\frac{Q}{2Lhw_0}$. $L$ is the total length of the flow channel, and $w_0$ is the initial width of the channel. The varying width ($w$) is given by:

$$w = -w_0\frac{L}{x} \tag{2-24}$$

Finally, the WSR in this flow chamber can be written as:

$$\dot{\gamma}_{\mathrm{w}} = \left(\frac{d}{dz}\boldsymbol{v}\right)|_{z=0} = \frac{6}{h}\bar{\boldsymbol{v}}$$

$$\dot{\gamma}_{\mathrm{w}} = \frac{6}{h}|\bar{v}_x + \bar{v}_y|$$

$$\dot{\gamma}_{\mathrm{w}} = \frac{12C}{h}\sqrt{x^2 + y^2} \tag{2-25}$$

From (2-25), the WSR field is linearly decreasing along the length of the flow chamber along the centerline (i.e., $y = 0$). Note that $x$ starts from the negative side in this stagnation flow setup. Therefore, for convenience, letting $l = L + x$, (2-24) and (2-25) become:

$$w = w_0 \frac{L}{L - l} \tag{2-26}$$

$$\dot{\gamma}_{\mathrm{w}}|_{y=0} = \frac{-12\mu C}{hL}\left(1 - \frac{l}{L}\right) \tag{2-27}$$

## 2.6.2 Designs and Materials for Ultrasound-compatible Flow Phantoms

Flow phantoms are known as essential laboratory tools in the field of vascular ultrasound (Hoskins, 2008). They have been used as calibration platforms for clinical ultrasound scanners (Browne, 2014) and serve as investigative tools for the testing of novel vascular ultrasound techniques (Wong et al., 2009; Leow et al., 2015). Flow phantoms with well-defined geometries, mechanical properties, and acoustic properties can facilitate the interpretation of the experimental results and evaluation of various estimation performance.

Agar and gelatin-based materials have been used (Burlew, Madsen, Zagzebski, Banjavic, & Sum, 1980; Madsen, Zagzebski, & Frank, 1982) to fabricate flow phantoms. Particles such as cellulose, graphite or aluminum oxide are added to provide attenuation and scattering properties. However, it has been reported that gelatin-based phantoms are unstable with temperature variation, susceptible to microbial invasion, and difficult to achieve uniform distribution of scatters (Jaeger et al. 1981). Meanwhile, both gelatin- and agar-based phantoms are found lack of mechanical strength, so the flow phantoms are prone to rupture (Ramnarine, Anderson, & Hoskin, 2001).

Polyvinyl alcohol (PVA) is one of the widely used materials for ultrasound-compatible phantom fabrication. PVA can form into a hydrogel upon freeze-thaw cycles through the cross-

linking process (Stauffer & Peppast, 1992). The elastic modulus of the material can be adjusted by varying the number of freeze-thaw cycles. Apart from its ultrasound compatibility, it provides adequate strength to withstand physiological pressure, allowing a wide range of flow conditions. Also, the PVA-based phantoms have long-term stability. It has been reported that the PVA-based phantoms remain mechanically stable over a 7-month period (Duboeuf et al., 2009).

## 2.7 Chapter Summary

Due to the non-invasiveness, fast scanning capability, and accessibility offered by ultrasound imaging, several ultrasound-based techniques have been proposed for WSR estimation. These techniques include CFI method, spectral Doppler, and echo particle image velocimetry. However, tracking the WSR dynamics along the vessel walls within a full image view without using contrast agents has not been demonstrated yet. Making use of the high-frame-rate data acquisition technique and multi-angle Doppler vector estimation method, we may be able to quantify the WSR patterns with a high temporal resolution without compromising the spatial dimension or clinical safety. To evaluate the estimation accuracy and sensitivity of a new WSR estimation method, we would need a flow chamber that can provide a spatially varying WSR pattern. A Hele-Shaw flow model which can generate a linear WSR field could serve this purpose well. Also, the material used for constructing the flow chamber should be ultrasound-compatible and provide sufficient mechanical strength. In this context, PVA-based flow phantoms have been proposed to act as the tissue mimicking material for constructing flow phantom models.

# CHAPTER 3

# Quantification of Wall Shear Rate using High-frame-rate Ultrasound Imaging Method

## 3.1 Chapter Overview

This chapter presents the imaging and experimental methods for the proposed WSR estimation algorithm. Section 3.2 illustrates the imaging procedures for acquiring high-frame-rate ultrasound data to compute the flow vectors. Section 3.3 introduces the proposed WSR estimation scheme based on the generated vector maps. Section 3.4 outlines the calibration test of the WSR estimation on a linear WSR field flow chamber. The settings for the CFD simulations are included. Section 3.5 covers the performance studies of the spatiotemporal WSR mapping using anthropomorphic flow phantoms. The model designs, fabrication protocols, and the experimental setups of the models used in Section 3.4 and 3.5 are discussed in the corresponding section.

## 3.2 High-frame-rate Ultrasound Data Acquisition

### 3.2.1 Imaging Hardware

The WSR estimation was performed using a research purpose, channel-domain imaging research platform available in our laboratory. The platform consists of: (1) a fully programmable front-end core (SonixTouch; Analogic Ultrasound, Peabody, MA, USA) which allows customization on the transmission and reception operations of each array element, (2) a multi-channel pre-beamformed data acquisition tool (Cheung et al., 2012). The acquired data were streamed to a back-end computing workstation that leverages GPU technology (So, Chen, Yiu, & Yu, 2011; Yiu, Tsang, & Yu, 2011) for further data processing. A 128-element linear array transducer (L14-5/38; Analogic

Ultrasound) was used for ultrasound transmission and reception. Detailed parameters of the imaging platform are listed in Table 3.1a.

| | Parameter | Value |
|---|---|---|
| **(a)** | **Imaging platform** | |
| | Number of elements | 128 |
| | Array pitch | 0.3048 mm |
| | Number of Tx/Rx channels | 128 |
| | Pre-beamformed data sampling rate | 40 MHz |
| | Pre-beamformed data bit resolution | 12 |
| **(b)** | **Data acquisition** | |
| | Imaging centre frequency | 5 MHz |
| | Tx pulse duration | 3 cycles |
| | Steering angles | -10°, 0°, +10° |
| | Pulse repetition frequency, $f_{PRF}$ | 10 kHz |
| | Effective data acquisition rate, $f_{DAQ}$ | 3.3 kHz |
| | Data acquisition duration | 1 s |
| **(c)** | **Slow-time data processing** | |
| | Normalized clutter filter cut-off frequency, $f_{cutoff}$ | 0.04 |
| | Filter design method | Equiripple, minimum order |
| | Filter order | 224 |
| | Stop-band suppression | 100 dB |
| | Sliding window for flow estimation | 64 samples |
| | Sliding window step size | 8 samples |

Table 3.1. Imaging parameters for high-frame-rate data acquisition.

## 3.2.2 Data Acquisition

To achieve adequate temporal resolution and acquire sufficient data for a consistent flow velocity vector estimation, we adopted the plane wave transmission technique to acquire high-frame-rate data. The transmit-firing sequence was programmed using the TEXO software development kit (Analogic Ultrasound) to transmit unfocused plane waves (three pulse cycles; $f_c$ = 5 MHz) from different steering angles. In this work, three Tx-Rx steering angle pairs (-10°, 0°, +10°) were chosen. According to the previous study (Yiu & Yu, 2016), this combination can yield consistent flow vector

estimates (both magnitude and flow directions) effectively. Other imaging parameters for the data acquisition are listed in Table 3.1b.

### 3.2.3 Receive Beamforming

The acquired RF data were streamed offline to the back-end processor. First, an FIR bandpass filter (cut-off frequencies: 3 and 7 MHz) was applied to the pre-beamformed data to improve the SNR. The cut-off frequencies were determined by the transmit center frequency, $f_c$ which was 5 MHz in this setup. Next, Hilbert Transform was performed to compute the analytic signal for the RF data. After that, beamforming was performed using a GPU-based delay-and-sum algorithm for plane wave transmission scheme that was developed previously by our lab (Yiu et al., 2011). In general, receive beamforming computes the depth information by resolving the time delays of the echo received by each array element. For example, the echo reflected from deeper tissue takes a longer time to return to the transducer. Based on the time delay and the estimated speed of sound in the imaging medium (typically assumed to be 1540 $ms^{-1}$), the intensity and the phase information (for Doppler frequency estimation) at the corresponding pixel position on an image can be computed using geometrical principles. Since multiple Tx-Rx angles were used, there were multiple beamformed images (LRIs) available for compounding. Here, three beamformed LSIs were compounded to form one HRI. In this study, each pixel in the data frames was 0.1×0.1 mm in size. These data frames were then passed to the flow processor to compute the flow vectors.

### 3.2.4 Velocity Map Generation

Clutter filtering was first applied to the data to suppress the unwanted tissue noises. A $224^{th}$ order FIR filter with 100 dB stop-band suppression was used. The filter design was based on ripple minimum-order method. Based on *ad hoc* evaluation of the clutter suppression performance, its normalized cutoff frequency was set to 0.04. The filtered data were then processed using the least-square vector computation method developed earlier by our lab (Yiu & Yu, 2014).

A slow-time ensemble window was defined over a group of filtered data at each pixel position. The mean frequency shift over an ensemble was computed using the well-established lag-one autocorrelation phase algorithm (Evans, 2010). A sliding window strategy was used to compute the mean frequency shift for each ensemble. In the current work, the ensemble size was set to 64 and the sliding window moved by eight samples each time. As there were nine Tx-Rx angle pairs in total, nine frequency estimates were available at each pixel position.

The vectors were then computed using the least-square approach as described in Subsection 2.4.2. In this 3-Tx and 3-Rx steering angles setup, the angles in (2-10a) became: $\varphi_{\mathrm{T}} = [-10, 0, 10]$ and $\varphi_{\mathrm{R}} = [-10, 0, 10]$. Therefore, nine linear equations were available to determine the axial and lateral vector components (i.e., $v_z$ and $v_x$) with the least mean-squared error.

## 3.3 Wall Shear Rate Quantification

### 3.3.1 Determining Tangent Vectors at Wall Positions

***Theory of wall orientation computation***

As discussed earlier, WSR is equivalent to the tangential velocity gradient at the vessel wall. Since most of the arteries are curved in nature (e.g., carotid bifurcation), the tangential directions along the vessel wall cannot be assumed constant. Hence, the tangent vectors at the vessel wall positions must be determined. The wall positions were first identified by manually tracing the vessel walls in the ultrasound B-mode image. Next, sliding neighbourhood operations were performed as follows. Each wall position pixel was defined as the centre pixel, and the neighbourhood represents its nearby pixels within a rectangular block. After that, the region properties of the block of pixels were exploited to determine the local orientation of the vessel wall within the block. This algorithm found an ellipse that gives the equivalent second spatial moments to the block of pixels, as shown in Fig. 3.1.

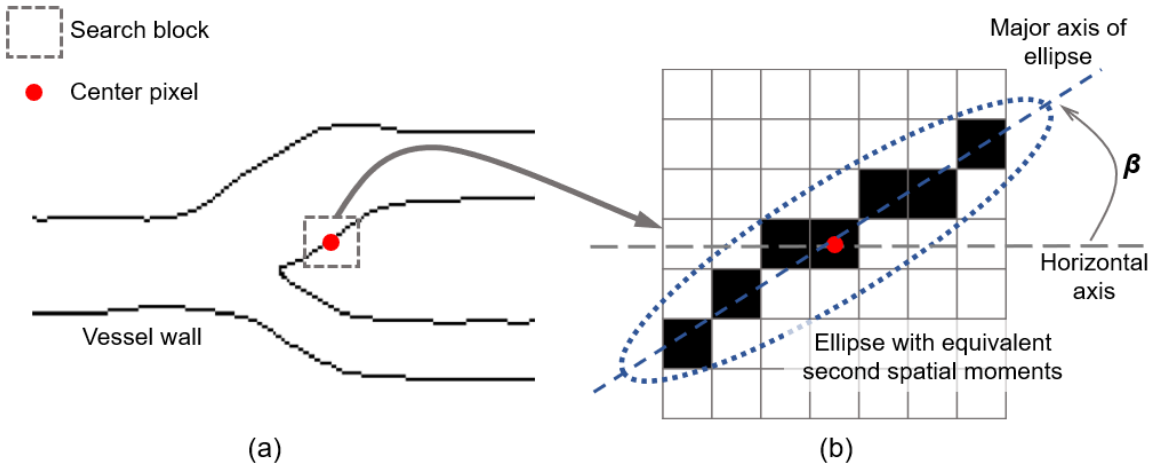


Fig. 3.1. Schematic illustration of the tangent vector computation at the vessel wall positions. (a) The wall position pixel and its surrounding pixels are selected to perform the region properties analysis. (b) The tangent vector with angle $\beta$ is computed by finding an ellipse with the equivalent second spatial moment.

The set of pixels in the block is denoted by *B*. The area of the block *A* and centroid $(\bar{r}_p, \bar{c}_p)$ are defined by:

$$A = \sum_{(r_p,c_p)\in B} 1$$
$$\bar{r}_p = \sum_{(r_p,c_p)\in B} r_p \qquad (3\text{-}1)$$
$$\bar{c}_p = \sum_{(r_p,c_p)\in B} c_p$$

where $(r_p,c_p)$ is the coordinates of the pixels within the pixel block *B*. There are three second-order spatial moments of the region *B*: second-order row moment $\mu_{rr}$, second-order mixed moment $\mu_{rc}$, second-order column moment $\mu_{cc}$:

$$\mu_{rr} = \frac{1}{A}\sum_{(r_p,c_p)\in B} (r_p - \bar{r}_p)^2$$
$$\mu_{rc} = \frac{1}{A}\sum_{(r_p,c_p)\in B} (r_p - \bar{r}_p)(\bar{c}_p - \bar{c}) \qquad (3\text{-}2)$$

$$\mu_{cc} = \frac{1}{A} \sum_{(r_p, c_p) \in B} (\bar{c}_p - \bar{c})^2$$

It has been shown that the properties of the major axis of the ellipse can be found using the three quantities above (Haralick & Shapiro, 1992). The aim is to find the angle between the major axis of the ellipse and the horizontal axis ($\beta$). There are four cases to be considered:

1. if $\mu_{rc} = 0$ and $\mu_{rr} > \mu_{cc}$, $\beta = -90°$

2. if $\mu_{rc} = 0$ and $\mu_{rr} \leq \mu_{cc}$, $\beta = 0°$

3. if $\mu_{rc} \neq 0$ and $\mu_{rr} \leq \mu_{cc}$,

$$\beta = \tan^{-1}\left\{\frac{-2\mu_{rc}}{\mu_{rr} - \mu_{cc} + [(\mu_{rr} - \mu_{cc})^2 + 4\mu_{rc}^2]^{1/2}}\right\}$$

4. if $\mu_{rc} \neq 0$ and $\mu_{rr} > \mu_{cc}$,

$$\beta = \tan^{-1}\left\{\frac{\{\mu_{rr} + \mu_{cc} + [(\mu_{rr} - \mu_{cc})^2 + 4\mu_{rc}^2]^{1/2}\}^{1/2}}{-2\mu_{rc}}\right\} \qquad (3\text{-}3)$$

Suppose a block of size $b \times b$ was chosen. The block length $b$ was determined based on three factors. First, the radius of the curvature of the vessel wall should be greater than $b/4$ so that the algorithm can identify the correct ellipse within the block (i.e., the imaginary circle needs to be larger than a quarter of the block. Second, the smallest separation between vessel walls should be greater than $b/2$ so that the block will not capture more than one vessel wall at a time. Lastly, the block should be sufficiently large so that it is less sensitive to the noises in the image. Based on the model geometries used in the flow experiments (to be discussed in Section 3.4 and 3.5), a 9×9 pixel block (0.9×0.9 mm) was chosen. Hence, the smallest radius of the curvature and the smallest wall separation that the block can resolve were 0.225 mm and 0.45 mm respectively. According to Lauric, Safain, Hippelheuser, and Malek (2014), the average radius of curvature found in the carotid arteries of healthy adults is about 6.6 mm. On the other hand, the smallest separation between vessel walls often

depends on the severity of the stenosis. It has been reported that 99% stenosis can be found in severe cases (Johnson, Verlato, Bergelin, Primozich, & Strandness, 1995). With the average diameter of human ICA, i.e., 4.2 mm as reported by Krejza et al. (2006), the 9×9 block is still a valid choice when the degree of stenosis is up to 89%. If a higher degree of stenosis is expected, a smaller pixel block should be used.

***Validation study***

A validation study was conducted to examine the accuracy of the tangent vector estimation. A circle of a radius of 50 pixels was generated using Matlab (R2016a; Mathworks, Natick, MA, USA). It was a binary map where the edge of the circle was set to 1, and the rest of the pixels were set to 0. The tangent directions along the perimeter of the circle were estimated using the abovementioned algorithm with a 9×9 search block. Reference values of the tangent directions of the same circle were calculated using geometrical principles. The errors produced by the estimation were quantified by computing the difference between the magnitude of the reference and estimated values.

## 3.3.2 Regularization of Velocity Profiles

As mentioned earlier, the near-wall flow velocity estimates are significantly affected because of the clutter filtering procedure. The incorrect near-wall flow vectors would give rise to inaccurate WSR estimation. The proposed method involves simultaneous smoothing and interpolation of the velocity maps based on the unaffected flow velocity vectors and the detected wall positions. The threshold of the clutter-affected flow velocities is denoted by $v_{\text{clutter}}$, which means that the velocity estimates lower than this value are expected to be influenced by the clutter filtering. Deriving from the Doppler equation (2-4), $v_{\text{clutter}}$ is given by:

$$v_{\text{clutter}} = \frac{c_0 f_{\text{cutoff}}}{4 \cos \theta_{\max}} \tag{3-4}$$

where $f_{\text{cutoff}}$ is the normalized cut-off frequency of the clutter filter applied, and $\theta_{\max}$ is the maximum beam-flow angle ($\theta_{\max} = 80°$ in this study). From the acquired flow vector maps, the velocity estimates

lower than $v_{\text{clutter}}$ were removed. Based on the no-slip boundary condition, the velocity estimates at the detected wall positions were enforced to be zero. However, the random noise in the estimated velocities would significantly affect the reconstruction and WSR estimation in the later stages. Therefore, it is necessary to perform smoothing operation on the flow vector maps to increase the robustness of the estimation. The two tasks here, vector map reconstruction and smoothing, were accomplished using an automated, penalized least-square regression algorithm (Garcia, 2010; Garcia, 2011).

***Theory of vector map smoothing***

Consider the simplest 1-D case:

$$x = \hat{x} + \varepsilon \tag{3-5}$$

where $x$ represents the noisy signal resulted from the smooth signal $\hat{x}$ and a Gaussian noise ε with zero mean and unknown variance. The penalized least-squares regression seeks to minimize the cost function $f(\hat{x})$:

$$f(\hat{x}) = \|\hat{x} - x\|^2 + s \cdot p(x) \tag{3-6}$$

where $p$ is a penalty term that indicates the roughness of the smooth data, and $s$ is a smoothing parameter controls the degree of smoothing. The term $\|\hat{x} - x\|^2$ is the residual-sum-of-squares between the smooth data and the noisy signal. Using a second-order divided difference (Weinert, 2007; Whittaker, 1923), the penalty term can be expressed in:

$$p(\hat{x}) = \|\mathrm{D}\hat{x}^2\| \tag{3-7}$$

where D is a square matrix defined by the number of elements $k$ and the step $h_k$ between $\hat{x}_k$ and $\hat{x}_{k+1}$, defined by: $\mathrm{D}_{k,k-1} = -\mathrm{D}_{k,k} = (h_{k-1}^2)^{-1}$. Hence, $f(\hat{x})$ can be minimized by taking the derivative of (3-6) with respect to $\hat{x}$, giving:

$$(\mathrm{I} + s\mathrm{D}^T\mathrm{D})\hat{x} = x \tag{3-8}$$

where I is a k×k identity matrix. (3-8) can be efficiently solved using inverse matrix method. As *s* has a strong influence on the outcome of the smoothing, an inappropriate choice of *s* will lead to over- or undersmoothing. Hence, the best value of *s* is determined using generalized cross-validation (GCV) method (Craven & Wahba, 1978; Wahba, 1990). This GCV method chooses the value of *s* that minimizes the GCV score, which can be written as:

$$\mathrm{GCV}(s) = \frac{\|\hat{x} - x\|^2/k}{(1 - Tr(\mathrm{H})/k)^2} \tag{3-9}$$

where $\mathrm{H} = (I + s\mathrm{D}^T\mathrm{D})$.

According to Garcia (2010), the smoothed output $\hat{x}$ can be written as:

$$\hat{x} = \mathrm{IDCT}(\Gamma\mathrm{DCT}(x)) \tag{3-10}$$

given a gridded dataset. DCT and IDCT denote the discrete cosine transform and its inverse respectively. The GCV score in (3-9) can also be expressed in:

$$\mathrm{GCV}(s) = \frac{k\sum_{i=1}^{k}(\frac{1}{1+s\lambda_i^2} - 1)^2\mathrm{DCT}\{x\}}{(k - \sum_{i=1}^{k}\frac{1}{1+s\lambda_i^2})^2} \tag{3-11}$$

where $\lambda_i^2$ is the eigenvalues of $\mathrm{D}^T\mathrm{D}$.

***<u>Theory of velocity profile interpolation</u>***

As mentioned earlier, the velocity estimates that are lower than the threshold $v_{clutter}$ will be removed. A weighting term (*W*) is added to deal with these removed data points. The minimized cost function (3-8) becomes:

$$(W + s\mathrm{D}^{\mathrm{T}}\mathrm{D})\hat{x} = Wx \tag{3-12}$$

where $W = 0$ for the removed data points and $W = 1$ for the valid data points (i.e., velocities higher than $v_{\mathrm{clutter}}$). (3-10) then becomes:

$$\hat{x}_{k+1} = \mathrm{IDCT}(\Gamma \mathrm{DCT}(W(x - \hat{x}_k) + \hat{x}_k) \tag{3-13}$$

where $\hat{x}_k$ refers to $\hat{x}_k$ calculated at the $k^{th}$ iteration step. The GCV score is given by:

$$\mathrm{GCV}(s) = \frac{\left\| W^{1/2}(\hat{x} - x) \right\|^2 / (k - k_{\text{removed)}}}{(1 - Tr(\mathrm{H})/k)^2} \tag{3-14}$$

where $k_{\text{removed}}$ represents the number of removed data points. The algorithm starts with assigning an arbitrary value for *s*. The calculation (3-13) repeats until GCV*(s)* converges to its minimum. This operation simultaneously smooths and interpolates the velocity maps. Hence, the interpolated velocity profiles are optimized in the sense that its mean-squared error is minimized and the best smooth. DCT can be easily extended to higher dimensions because a multidimensional DCT is simply a separable product of DCTs along each dimension.

***Validation Study***

A validation study was performed to evaluate the effectiveness of using this method to reconstruct the velocity profiles. Velocity profiles were constructed based on the following formula:

$$\tilde{v} = 1 - \left| \frac{r}{R} \right|^n \tag{3-13}$$

where $\tilde{v}$ is the normalized velocity with maximum value = 1, and n is the degree of flattening of the velocity profile.

It has been found that *n* varies from 2 to 4 in arterial blood flow (Reneman, Woldhuis, Egbrink, Slaaf, & Tangelder, 1992; Tangelder et al., 1986), including systole and diastole phase. Therefore, velocity profiles were generated using (3-13) with n = 2 to 4. To simulate the rejection of clutter-filter affected data, velocity data points that were lower than a defined threshold value were deliberately removed. In this work, four threshold values (0.1, 0.3, 0.5, and 0.7) were selected. The velocities at the wall position (i.e., $v(r = \mathrm{R})$) were kept at zero according to the no-slip condition. After that, the DCT-based penalized least-squares algorithm was applied to the data to perform the regularization of the vector maps. The errors of the reconstruction procedure were quantified by

calculating the root-mean-squared error (RMSE) between the original profiles and the reconstructed ones.

### 3.3.3 Velocity Gradients Mapping

Sobel-Feldman filter (or simply Sobel filter) was implemented to compute the velocity gradient map from the flow vector map. Sobel filter is a widely used operator for edge detection in imaging processing (Sobel & Feldman, 1968). The smallest kernel size for Sobel filter is 3×3. The filter consists of two kernels for horizontal and vertical directions, which are denoted by $K_{x,3}$ and $K_{z,3}$ respectively:

$$\mathrm{K}_{x,3} = \frac{1}{8}\begin{bmatrix} 1 & 0 & -1 \\ 2 & 0 & -2 \\ 1 & 0 & -1 \end{bmatrix}$$

$$\mathrm{K}_{z,3} = \mathrm{K}_{x,3}^{T} = \frac{1}{8}\begin{bmatrix} 1 & 2 & 1 \\ 0 & 0 & 0 \\ -1 & -2 & -1 \end{bmatrix} \tag{3-14}$$

In edge detection application, the coefficient 1/8 is often omitted because only the edge features of the image are of interest. However, the coefficient in WSR quantification is necessary to obtain the correct magnitude of the velocity gradient. The 3×3 kernel can be seen as the convolution of a smoothing kernel and a gradient kernel. For example, for $K_{x,3}$:

$$\mathrm{K}_{x,3} = \frac{1}{8}\begin{bmatrix} 1 & 0 & -1 \\ 2 & 0 & -2 \\ 1 & 0 & -1 \end{bmatrix} = \frac{1}{8}\begin{bmatrix} 1 \\ 2 \\ 1 \end{bmatrix}\begin{bmatrix} 1 & 0 & -1 \end{bmatrix} \tag{3-15}$$

The column vector is a triangle filter that carries out smoothing perpendicular to the derivative direction. The row vector is a central difference operator that approximates the gradient. Sobel filter with a larger kernel size can be obtained by convolving the kernel with another smoothing kernel:

$$\mathrm{K}_{x,5} = \begin{bmatrix} 1 \\ 2 \\ 1 \end{bmatrix}\begin{bmatrix} 1 & 2 & -1 \end{bmatrix} * \mathrm{K}_{x,3}$$

$$\mathrm{K}_{x,7} = \begin{bmatrix}1\\2\\1\end{bmatrix}[1 \quad 2 \quad -1] * \mathrm{K}_{x,5} \tag{3-16}$$

In a generalized form:

$$\mathrm{K}_{x,p} = \left(\begin{bmatrix}1\\2\\1\end{bmatrix}[1 \quad 2 \quad -1]\right)^{*(p-3)} * \mathrm{K}_{x,3} \tag{3-17}$$

where $p$ = 3, 5, 7, …etc. $\mathrm{K}_{y,p}$ can be obtained similarly, or simply taking the transpose of $\mathrm{K}_{x,p}$.

Although using a larger kernel would give a more consistent gradient estimation because of a stronger smoothing power, it could introduce underestimation to the WSR estimation. It is because the near wall gradient is normally greater than one (i.e., concave), a first-order gradient approximation with a larger window leads to a more significant underestimation on the gradient. In this work, 5×5 kernels were chosen to balance the estimation consistency and the accuracy. As described above, the two kernels of a 5×5 Sobel filter are given as follows:

$$\mathrm{K}_{x,5} = \frac{1}{108}\begin{bmatrix}1 & 2 & 0 & -2 & -1\\4 & 8 & 0 & -8 & -4\\6 & 12 & 0 & -12 & -6\\4 & 8 & 0 & -8 & -4\\1 & 2 & 0 & -2 & -1\end{bmatrix}$$

$$\mathrm{K}_{z,5} = \frac{1}{108}\begin{bmatrix}1 & 4 & 6 & 4 & 1\\2 & 8 & 12 & 8 & 2\\0 & 0 & 0 & 0 & 0\\-2 & -8 & -12 & -8 & -2\\-1 & -4 & -6 & -4 & -1\end{bmatrix} \tag{3-18}$$

The two Sobel filter kernels, $\mathrm{K}_{x,5}$ and $\mathrm{K}_{z,5}$, were applied to the velocity vector maps, $\mathbf{V_x}$ and $\mathbf{V_z}$. It yields four velocity gradient maps:

$$\mathbf{G}_{xx} = K_{x,5} * \mathbf{V}_x$$

$$\mathbf{G}_{xz} = K_{z,5} * \mathbf{V}_x$$

$$\mathbf{G}_{zz} = K_{z,5} * \mathbf{V}_z$$

$$\mathbf{G}_{zx} = K_{x,5} * \mathbf{V}_z \tag{3-19}$$

where $\mathbf{G}_{ij}$ denotes the *i*-direction gradient of the *j*-direction velocity vector map (i.e., $\mathbf{V}_j$).

### 3.3.4 Coordinate Transforms of Shear Rate Tensors

Since the WSR represents the tangential velocity gradient at the wall positions, the tangential components of the velocity gradient maps at the detected wall positions need to be obtained. This operation is known as a 2-D coordinate transformation because the shear rate is a second rank tensor (Roark, Young, & Budynas, 2002). The shear rate tensor (also known as rate-of-shear tensor) $S_{ij}$ in a 2-D Cartesian coordinate system can be defined by (Currie, 2013):

$$S_{ij} = \frac{\partial v_i}{\partial x_j} + \frac{\partial v_j}{\partial x_i} \tag{3-20}$$

The coefficient 1/2 has been omitted here since it will be cancelled out in the transformation operation. Also, $S_{xz} = S_{zx}$ from (3-20) since rate-of-shear tensor is symmetric.

In matrix form, it can be written as:

$$\mathbf{S}_{ij} = \mathbf{G}_{ij} + \mathbf{G}_{ji} \tag{3-21}$$

The pixel positions of the detected vessel wall are denoted by ($m_w$,$n_w$). The transformation can be carried out as follows:

$$\begin{bmatrix} S_{x'x'}(m_\mathrm{w}, n_\mathrm{w}) & S_{x'z'}(m_\mathrm{w}, n_\mathrm{w}) \\ S_{z'x'}(m_\mathrm{w}, n_\mathrm{w}) & S_{z'z'}(m_\mathrm{w}, n_\mathrm{w}) \end{bmatrix} = \mathbf{Q} \begin{bmatrix} S_{xx}(m_\mathrm{w}, n_\mathrm{w}) & S_{xz}(m_\mathrm{w}, n_\mathrm{w}) \\ S_{zx}(m_\mathrm{w}, n_\mathrm{w}) & S_{zz}(m_\mathrm{w}, n_\mathrm{w}) \end{bmatrix} \mathbf{Q}^{\boldsymbol{T}} \tag{3-33}$$

where $x'$ and $z'$ represent the rotated coordinate system, as shown in Fig. 3.2. **Q** is known as the rotation matrix:

$$\mathbf{Q} = \begin{bmatrix} \cos\beta(m_\mathrm{w}, n_\mathrm{w}) & \sin\beta(m_\mathrm{w}, n_\mathrm{w}) \\ -\sin\beta(m_\mathrm{w}, n_\mathrm{w}) & \cos\beta(m_\mathrm{w}, n_\mathrm{w}) \end{bmatrix} \tag{3-34}$$

where $\beta$ is the angle defined in Subsection 3.3.1. From (3-33), the WSR $\dot{\gamma}_w$ at ($m_\mathrm{w}$,$n_\mathrm{w}$) is then:

$$\dot{\gamma}_w = S_{x'z'}(m_{\mathrm{w}}, n_{\mathrm{w}}) = S_{z'x'}(m_{\mathrm{w}}, n_{\mathrm{w}})$$
$$= [S_{zz}(m_{\mathrm{w}}, n_{\mathrm{w}}) - S_{xx}(m_{\mathrm{w}}, n_{\mathrm{w}})] \sin\beta \cos\beta \qquad (3\text{-}35)$$
$$+S_{xz}(m_{\mathrm{w}}, n_{\mathrm{w}})(\cos^2\beta - \sin^2\beta)$$

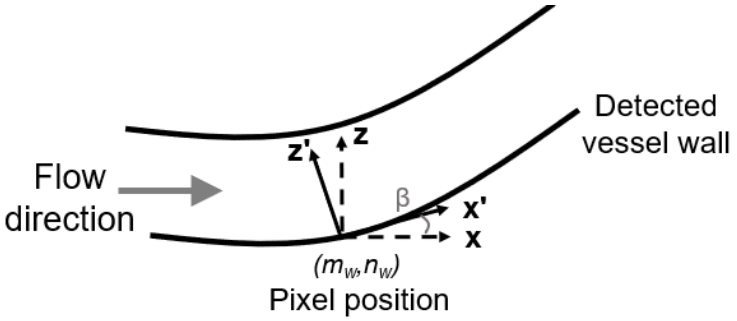


Fig. 3.2. Schematic illustration of the coordinate transformation based on the tangent vector.

# 3.4 Linear Wall Shear Rate Flow Chamber for Calibration

## 3.4.1 Model Design

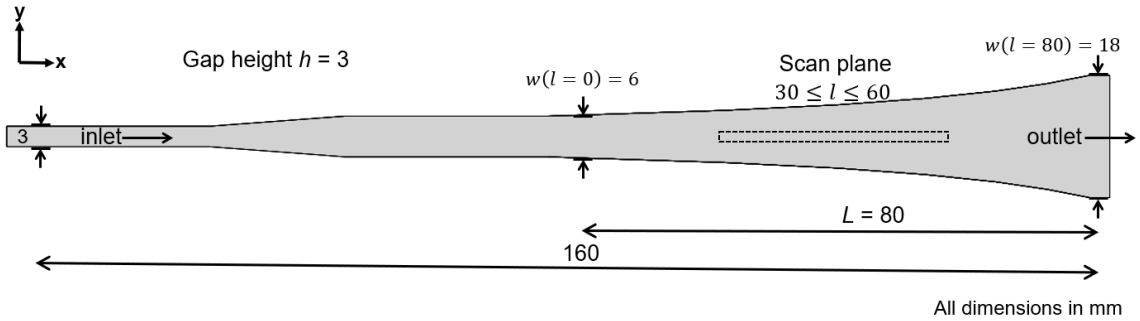


Fig. 3.3. CAD drawing of the Hele-Shaw flow chamber for a linear WSR field. Outer dimension: 160×18×3 mm. The ultrasound probe was placed at $30 \leq l \leq 60$ mm, and the scan plane was parallel to the x-z plane along the centerline of the flow chamber.

A Hele-Shaw flow chamber that can generate a linear WSR field was used to evaluate the accuracy of the WSR estimation algorithm. The geometry and dimensions of the flow chamber are shown in Fig. 3.3. The total length of the flow chamber is 160 mm. It has a constant gap height ($h$) of 3 mm. The entrance width of the chamber is 3 mm. The width increases to 6 mm and remains constant

until the midpoint of the flow chamber. This front part of the chamber is designed for two purposes: (i) create a fully developed flow before the flow entering the imaging region, and (ii) eliminate any flow disturbance caused by the flow connectors at the inlet. The linearly decreasing WSR region starts from $l = 0$ to $l = 80$. The scan plane for the imaging experiments started from $l = 0$ to $l = 80$, and was aligned to the centerline of the chamber. Following the derivation results (2-26), the channel width, *w*, in $0 \leq l \leq 80$, slowly expands by $w(l) = \frac{480}{80-l}$ mm. At the outlet, the exit channel width is 18 mm. In this study, three flow rate setups: 1.5 mL/s, 3.0 mL/s, and 4.5 mL/s were studied. Reynolds numbers based on the hydraulic diameter at $l = 0$ for the 1.5 mL/s, 3.0 mL/s, and 4.5 mL/s setups were 84.3, 168.9, and 252.9 respectively. The Reynolds numbers were not particularly low for a Hele-Shaw flow due to several design considerations. First, the model geometries and flow rates were optimized to produce a WSS range from 0.39 – 2.01 Pa which covers the physiological WSS range (atherogenic < 0.4 Pa and atheroprotective > 1.2 Pa). Second, the material used for constructing an ultrasound-compatible flow chamber has finite bend strength. If the channel width *w* is too large, the flow chamber tends to collapse at the outlet side. Lastly, the gap height of the model should be comparable to the lumen diameter of human carotid arteries so that the calibration results of the WSR estimation can be relevant to its application on arterial imaging. $h$ = 3 mm was therefore chosen for this setup. After all, the ultimate goal of the model design is to achieve a linear WSR field within the imaging view. Therefore, the linearity of the WSR fields obtained from CFD simulation and imaging experiments was assessed.

### 3.4.2 Computational Fluid Dynamics Simulations

A computer-aided design (CAD) model with the geometry described in the last section was drafted using SolidWorks (Dassault Systemes, Waltham, MA, USA). The CFD simulations were performed using the Flow Simulation package in the software. The cell size was 0.13 mm in all dimensions. In total, approximately 130,000 cells were generated for the simulation. The mesh independence was checked by progressively refining the mesh until the simulation converged. The

fluid flow in the entire channel was simulated. Three volumetric flow rates were prescribed as the inlet boundary conditions: 1.5 mL/s, 3.0 mL/s, 4.5 mL/s. At the outlet, atmospheric pressure was chosen as the boundary condition. The no-slip condition enforced at the walls of the flow channel. The convergence of the simulation was determined by the difference between the average pressure at the inlet and outlet.

### 3.4.3 Phantom fabrication protocol

***Construction of Hele-Shaw flow model and casting parts***

A flow phantom based on the Hele-Shaw flow model was fabricated in-house *via* an investment casting approach that is similar to that described in our previous work (Ho et al., 2017). The Hele-Shaw flow model core was built using an open-source 3-D printer. The extruder head size was 0.25 mm, which also defined the print resolution in the horizontal direction. On the other hand, the layer thickness was set to 0.1 mm, which defined the print resolution in the vertical direction. Polylactic acid (PLA) was chosen as the print material.

To facilitate the construction of the flow phantoms, two side plates and a casting case were drafted using SolidWorks and 3-D printed (as shown in Fig. 3.4a). The function of the side plates was to fasten the two ends of the 3-D printed physical replicate. The casting case provided a well-defined volume for the flow phantom. For the current model, the inner dimensions of the casting case were 164×55×60 mm (length×width×height). Each side plate was 55×60 mm (length×width) in dimension and 3 mm in thickness. A rectangular void was created at 15 mm depth (from the top) for each side plate to suspend the core horizontally in the casting case. For the side plates, the dimension of the void was 3×3 mm and 18×3 mm for the inlet and outlet respectively. With the core fastened onto the side plates, they were slid into the casting case (as shown in Fig. 3.4b).

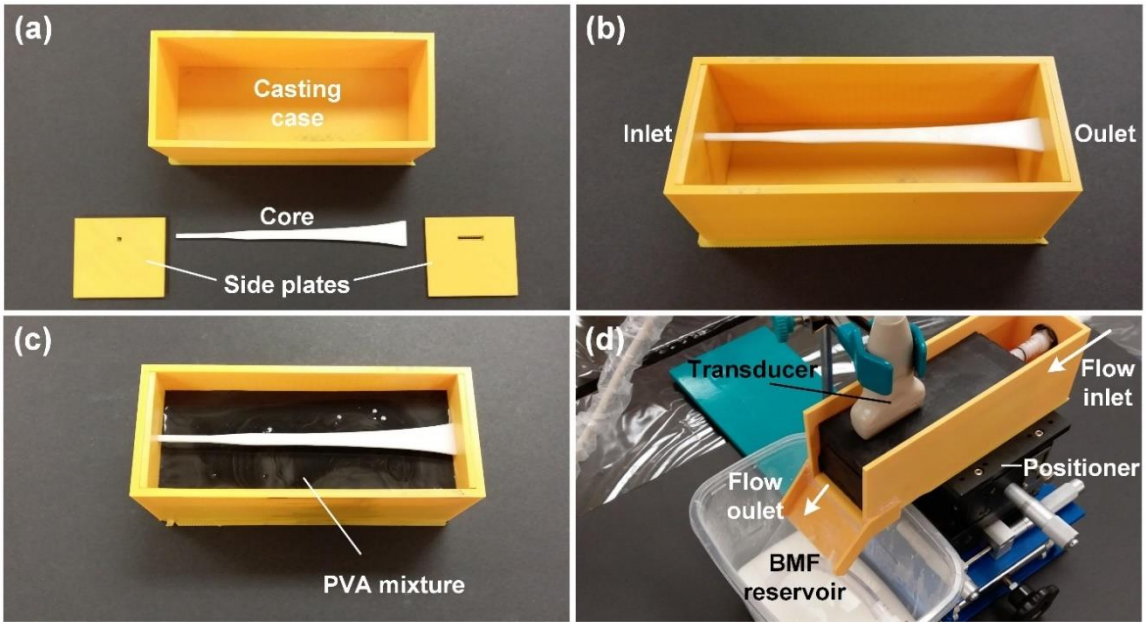


Fig. 3.4. (a) Key components involved in phantom construction: casting case, two side plates, and the Hele-Shaw flow model core. (b) Mounting of the core onto two side plates and placed within the casting case. (c) Casting case with the suspended core and the cavity half-filled with PVA mixture. (d) Setup for imaging experiments. The phantom was inserted into a phantom box placed on a positioner. The flow connector on the box was connected to the flow circuit with circulating BMF.

***Preparation of tissue mimicking material and cryogel formation***

PVA was selected as the tissue mimic for the flow phantom fabrication. The PVA mixture was prepared according to the following formula:

| Percentage (by weight) | Material | Manufacturer and part number |
|---|---|---|
| 10% | PVA powder | 341584; Sigma-Aldrich |
| 3% | Fine graphite particles | 282863; Sigma-Aldrich |
| 0.3% | Potassium sorbate | 85520; Sigma-Aldrich |
| 86.7% | Distilled water | N/A |

Table 3.2. PVA-based tissue mimicking material formulation.

The graphite particles were added to provide adequate attenuation similar to that found in human tissue. The potassium sorbate served as a preservative to provide long-term stability of the flow phantom. The materials were heated to 90°C and stirred until all the solids dissolved. After cooling

the mixture to room temperature, it was poured slowly into the casting case where the physical model was suspended inside (as shown in Fig. 3.4c).

Three freeze-thaw cycles were applied to develop the cryogel properties of the PVA mixture. For each freezing stage, the mixture together with the casting parts was placed in a freezer at -20°C for 24 hours; for each thawing cycle stage, it was placed in a refrigerator at 4°C for another 24 hours. During each freeze-thaw cycle, the PVA molecules would undergo crystallization, hence increasing the stiffness of the PVA cryogel (Surry, Austin, Fenster, & Peters, 2004).

After the freeze-thaw stage, the phantom was removed from the casting case. Then the core was retrieved from the PVA cryogel by gently pulling the core out from the outlet end. The inlet of the phantom was inserted into a 3-D printed imaging case with a quick-fit flow-tube connector attached to enable connection with the flow circuit.

***Acoustic compatibility of PVA-based flow phantoms***

As reported earlier (Ho et al., 2017), the experimentally derived acoustic speed and attenuation coefficient of the PVA-based phantom were shown as follows. As a comparison, the nominal acoustic properties of human tissue were also listed.

| **Parameters** | **PVA-based phantom** | **Human tissue** |
|---|---|---|
| Acoustic speed (m/s) | 1535 ± 2.4 | 1540 |
| Attenuation coefficient (dB/cm·MHz) | 0.229 ± 0.032 | 0.3-0.7 |

Table 3.3. Acoustic properties of PVA-based phantom and human tissue.

***Blood mimicking fluid fabrication***

A standardized formula was used to fabricate Blood mimicking fluid (BMF) with acoustic scattering and viscosity properties matched to those of human blood (Ramnarine, Nassiri, Hoskins, & Lubbers, 1998). The materials were added in the following order:

| **Percentage (by weight)** | **Material** | **Manufacturer and part number** |
|---|---|---|
| 83.7% | Distilled water | N/A |

| | | |
|---|---|---|
| 0.3% | Potassium sorbate | 85520; Sigma-Aldrich |
| 3.3% | Dextran | D4876; Sigma-Aldrich |
| 10% | Glycerol | 15514-029; Thermo Fisher Scientific |
| 0.9% | Tergitol | 86453; Sigma-Aldrich |
| 1.8% | Organsol | 2001 UD NAT1; Arkema |

Table 3.4. BMF formulation.

Glycerol served to tune the acoustic speed and density. Dextran was added to tune the fluid viscosity. Organsol was made of 5 μm diameter particles that served as ultrasound scatterers. Tergitol served as a surfactant that ensures a sufficient dispersion of the scattering particles. Potassium sorbate served as an anti-bacterial agent. The detailed fabrication procedure has been discussed in our previous work (Ho et al., 2017).

## 3.4.4 Flow Circuit Setup

***Overview of in-house flow pump system***

An in-house programmable flow pump system that developed earlier (Ho et al., 2017) was used to drive the operations of the phantom. It can allow the flow rate and flow pulse shape to be customized. The major components of the flow pump system included a gear pump, servo motor and motor driver, and an Arduino board. The inlet of gear pump was connected to a BMF reservoir which allows the BMF to enter the pump. The gear pump was driven by the servo motor. The speed of the motor (corresponding to the flow waveform and the flow rate) was determined by the pulsing frequency transmitted from the Arduino board. For every pulse sent by the Arduino board, the gear pump would rotate by 1/1000 revolution. The desired flow rate and waveform were specified by the user through an Arduino display panel.

***Flow Circuit Assembly***

The flow phantom was put into operation by connecting it to the flow pump system. First, the phantom was placed on a positioning stage that allows precise positioning. Next, the phantom's inlet was connected to the outlet of flow pump using the flexible vinyl flow tubing attached to quick-fit connectors. After that, the BMF reservoir was placed beneath the slide of the imaging case, so that

the fluid coming out from the phantom's outlet can be directed back to the reservoir. The setup was designed to ensure an atmospheric pressure at the flow outlet to match the boundary condition for the CFD simulations. The flow circuit assembly was as shown in Fig. 3.4d. After assembling the flow circuit, the flow pump was configured to drive a steady flow at 1.5 mL/s, 3.0 mL/s, and 4.5 mL/s. The ultrasound probe was aligned to the centerline to scan along the long axis of the phantom.

# 3.5 Anthropomorphic Flow Phantoms for Performance Investigation

## 3.5.1 Design of carotid bifurcation models

Anatomically realistic carotid bifurcation phantoms were designed and fabricated to investigate the performance of the proposed WSR estimation on resolving the WSR in complex flow dynamics. The carotid bifurcation models were designed based on a generalized tuning-fork co-planar vessel geometry (Smith, Rutt, & Holdsworth, 1999), which consists of three branches: common carotid artery (CCA) with 6 mm diameter, internal carotid artery (ICA) with 4.2 mm diameter, and external carotid artery (ICA) with 3.5 mm diameter. The vessel dimensions are defined in the way that they matched the mean carotid artery diameter of adults (Krejza et al., 2006). The merit of using such model is twofold. First, the model resembled the key geometrical features of human vasculature, so the applicability of the proposed method on the *in-vivo* study can be justified. Second, the shear stress pattern has been characterized by others using optical particle imaging velocimetry method (Kefayati et al., 2014), which is regarded as the ground truth. The results from those studies could serve as a reference for comparison with those obtained using the proposed method.

Two carotid bifurcation models were used in this study: (i) healthy model; (ii) diseased model with 50% eccentric stenosis at the ICA branch entrance. The dimension at the narrowing region in the diseased model was designed according to the North America Symptomatic Carotid

Endarterectomy Trial (NASCET) criteria (Smith, Rutt, Fox, & Rankin, 1996). The degree of stenosis is determined by the following formula:

$$\%\ \text{of ICA stenosis} = \frac{\text{Distal ICA diameter-Diameter at the site of maximal narrowing}}{\text{Distal ICA diameter}} \times 100\%$$

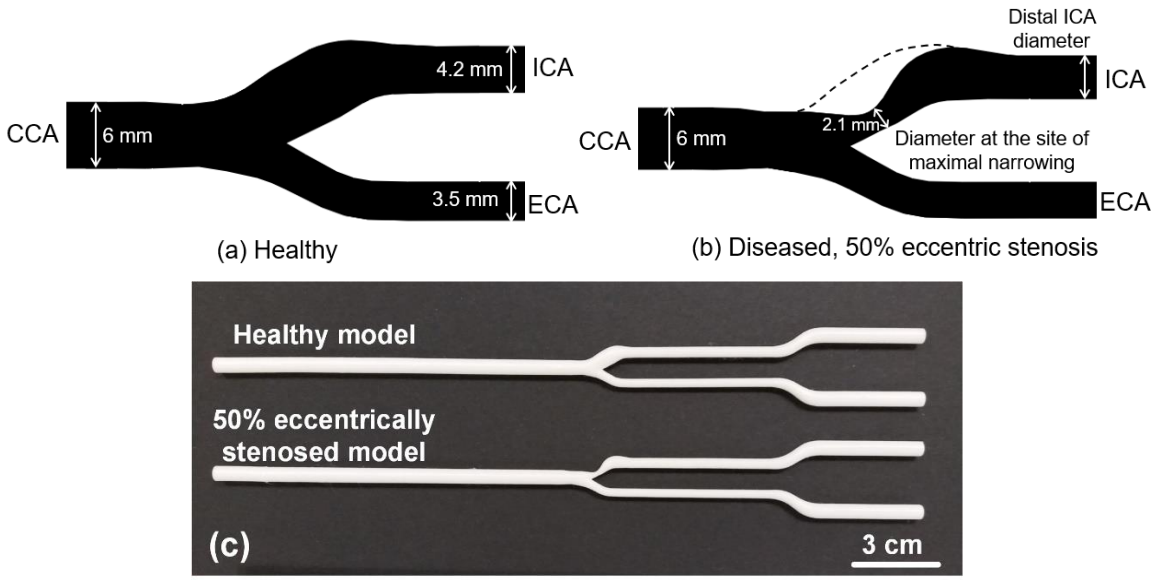


Fig. 3.5. Carotid bifurcation models according to NASCET criteria. (a) Geometry of healthy model. (b) Geometry of diseased model with 50% eccentric stenosis. (c) 3-D printed model cores of (a) and (b).

## 3.5.2 Carotid bifurcation flow phantoms fabrication

The fabrication protocol used here was similar to that described previously (see Subsection 3.4.3). CAD models of these carotid bifurcation models were drafted using SolidWorks. Note that the three branches (CCA, ICA, and ECA) were extended so that the core had a total length of 280 mm. The vessel cores, a casting case (280×60×60 mm), two side plates (60×60 mm) were 3-D printed (as shown in Fig. 3.6a). The vessel cores were printed with a lower infill density (12.5%) to facilitate the core removal procedure in the later stage.

After mounting the core onto the casting case, PVA mixture was poured into the case (as shown in Fig. 3.6b-c), followed by three freeze-thaw cycles. As the vessel core had a tuning-fork geometry, it cannot be directly pulled out from the phantom. As mentioned before, the vessel core was printed at a lower infill density; therefore, the vessel core was removed by gently snapping the core to break its mechanical structure and slowly retrieving the PLA fragments. The lumen of the phantom was then rinsed with water to remove any remaining PLA debris.

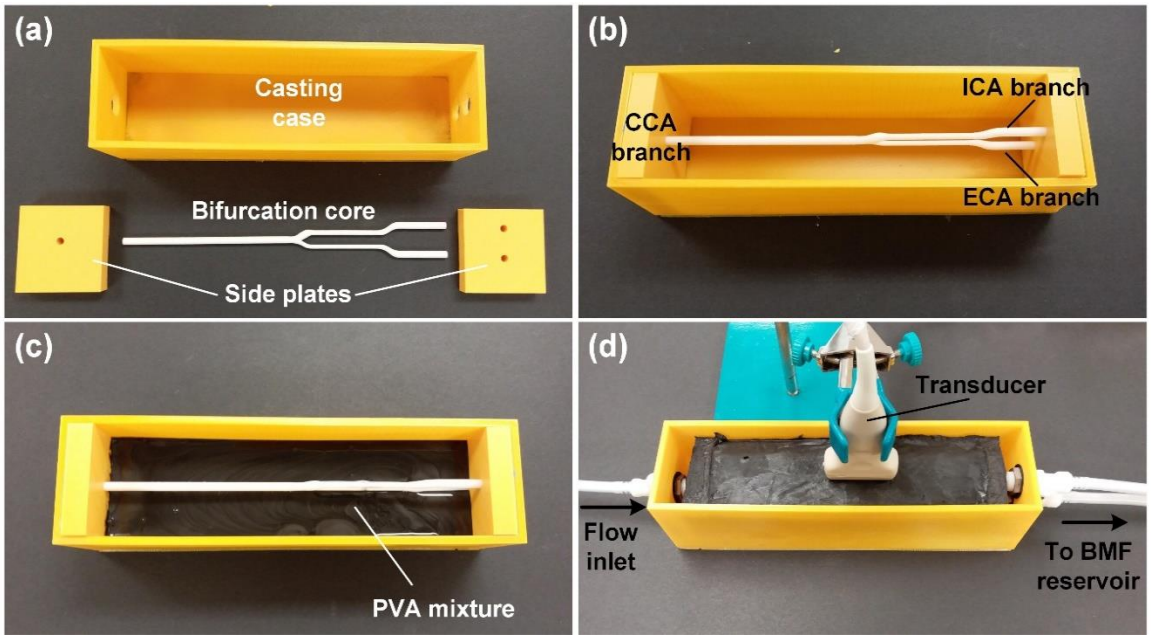


Fig. 3.6. (a) Key components involved in carotid bifurcation phantoms construction: casting case, two side plates, and the bifurcation model core. The healthy model was used as a demonstration. (b) Mounting of the core onto two side plates and placed within the casting case. The ICA branch and ECA branch were inserted into the upper and lower void of the side plate respectively. (c) Casting case with the suspended core and the cavity half-filled with PVA mixture. (d) Setup for imaging experiments. The phantom was inserted into a phantom box which was connected to the flow pump system.

## 3.5.3. Flow Circuit Setup

***Flow circuit assembly***

The CCA branch of the bifurcation phantom was connected to the outlet of the flow pump. The ICA and ECA branches were connected on two 2-mm-diameter flow resistors by vinyl flow

tubing (as shown in Fig. 3.6d). After the flow resistors, the two flow tubes were merged using a Y-junction connector; then the BMF was channelled back to the BMF reservoir. The flow pump was configured to deliver a pulsatile flow profile. The flow profile resembled several key features of the human carotid waveform as follows:

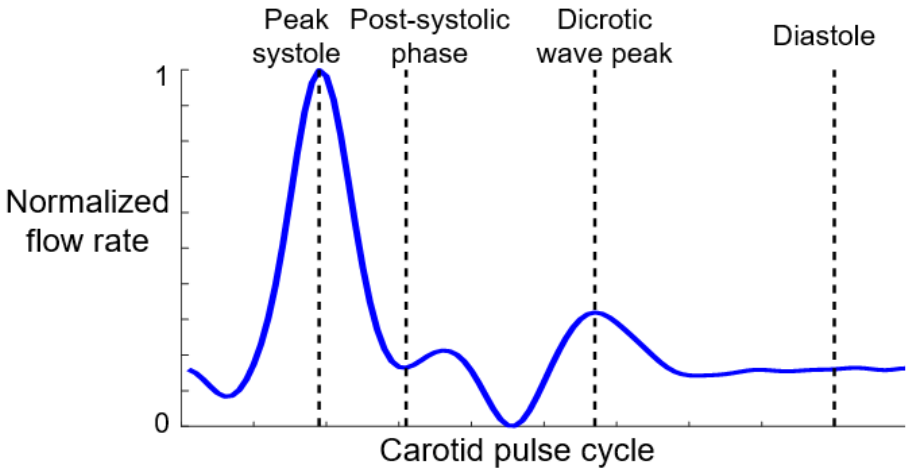


Fig. 3.7. Human carotid flow waveform. Four key phases: peak systole, post-systolic phase, dicrotic wave peak, and diastole were indicated.

The flow pump was set to drive the pulsatile flow at 1.0 Hz (i.e., 60 beats/min). The peak and mean flow rate were 8 ml/s and 1.95 ml/s respectively.

## 3.6 Chapter Summary

Regarding the imaging setup, the plane wave transmission scheme with 3 steering angles was adopted to acquire high-frame-rate ultrasound data ($f_{DAQ}$ = 3.3 kHz). The flow velocity vectors were obtained through two key operations: multi-angle Doppler analysis and least-squares vector estimation. After the data acquisition, the image frames were processed using the proposed WSR quantification technique.

First, the tangential directions at the detected wall positions were computed using a region properties analysis. The accuracy of the angle estimation was evaluated using a simulation study.

Next, the flow vectors within the flow region were first regularized using a DCT-based penalized least-square regression approach. This procedure was implemented to simultaneously smooth the flow velocity maps and interpolate the near-wall velocity profiles which were influenced by the cluttering filtering process. Its ability to reconstruct the velocity profiles was studied by implementing this algorithm on a ideal velocity profiles with portions of data removed. After that, a Hele-Shaw flow chamber was constructed to comprehensively evaluate the accuracy of the WSR estimation under three different flow rate setups. Finally, two carotid bifurcation phantom models (healthy model and diseased model) were built to demonstrate the capability of the proposed WSR estimation method to track the spatiotemporal WSR dynamics in complex flow dynamics.

# CHAPTER 4

# Experimental Results of Wall Shear Rate Estimation

## 4.1 Chapter Overview

Chapter 4 presents the results of the WSR estimation experiments. Section 4.2 reports the results for the estimation of tangent vectors at the wall positions. Section 4.3 shows the results of the regularization of velocity profiles. Section 4.4 examines the results of WSR estimation in the Hele-Shaw linear WSR flow chamber. Section 4.5 highlights the findings of the WSR measurements in the carotid bifurcation flow phantoms.

## 4.2 Computation of Tangent Vectors

***Validation study***

Fig. 4.1 illustrates the accuracy of the tangential direction estimation using a perfect circle. The radius of the circle was 50 pixels and a 9×9 search block was used. The angle $\beta$ computed using the formula (3-3) is within the range ±90°. In this particular configuration, the angle always starts from either 0° or 180° (i.e., vertical axis). The clockwise direction is defined as positive, while the anti-clockwise direction is defined as negative. The reference angles, estimated angles, and the differences between their magnitudes are shown in Fig. 4.1a, 4.1b, and 4.1c respectively. From Fig. 4.1c, most of the estimated angles only slightly differ from the analytic ones. The average percentage error is below 0.4%. The maximum estimation errors 6.5% are found near the 0° and ±90° positions. Note that based on transformation equation (3-35), if the angle is close to 0° and ±90°, the effect of the angle estimation error on the WSR calculation would be insignificant. The relationship between

the radius of the circle and the estimation error was not extensively studied. However, it is expected that the estimation error should be consistent for a circle geometry, as long as the radius is greater than 1/4 of the block size (as explained in Subsection 3.3.1). Note that the physical radius of the circle used was 5 mm (with pixel size 0.1×0.1 mm). Considering that the average radius of curvature found in healthy adults is approximately 6.6 mm (Lauric et al., 2014), the results of this study would be relevant and valid for the *in vitro* investigations later on.

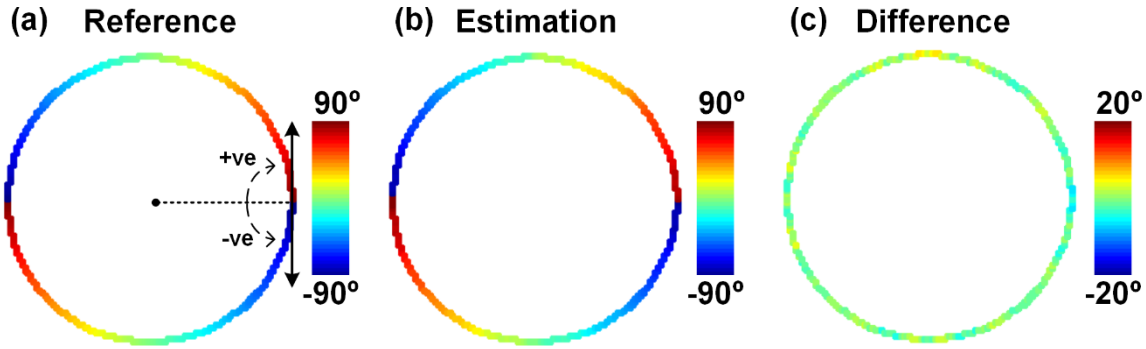


Fig. 4.1. (a) Reference values and (b) estimated values of the tangential directions (angle $\beta$) along the perimeter of a circle. (c) The differences between the magnitudes of (a) and (b).

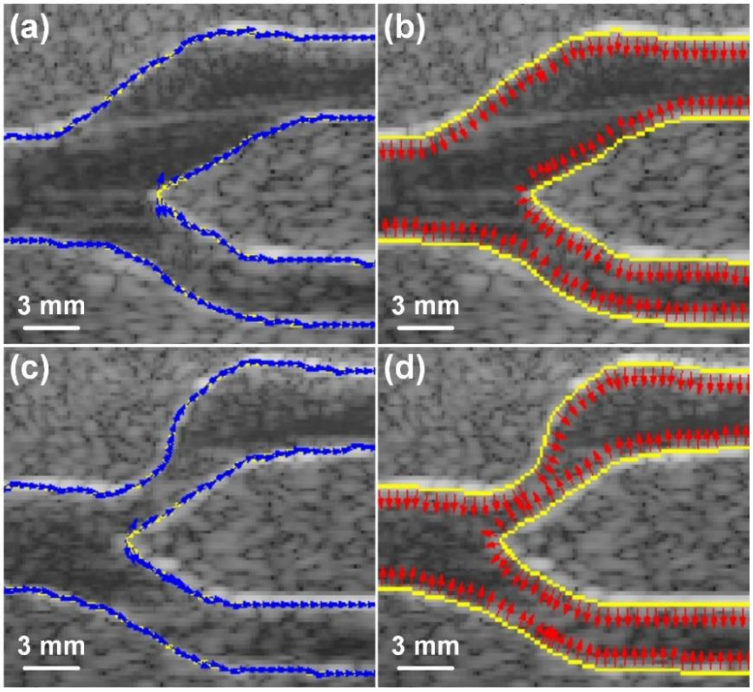


Fig. 4.2. Tangent vectors and normal vectors at the detected wall positions on the (a,b) healthy carotid bifurcation phantom and (c,d) 50% stenosed carotid bifurcation phantom.

***Flow phantom study***

The tangential direction estimation was applied to the carotid bifurcation models. The results are shown in Fig. 4.2. The yellow lines indicate the estimated vessel wall positions. The blue arrows in Fig. 4.2a&c (first column) illustrate the tangential directions along the vessel walls of the healthy model and 50% stenosed model respectively. For better visualization, the tangential vectors were rotated by 90° to show the normal vectors (red arrows) at the corresponding wall positions in Fig. 4.2b&d. They were rotated in a way that the normal vectors were pointing towards the flow region. Note that the vectors were plotted at every other wall position pixel so that the arrows can be seen clearly. From Fig. 4.4a&c, it can be observed that the curve formed by joining the tangential vectors follow the wall contours in general. Slightly higher deviations are observed on the vectors near the V-shaped bifurcation points. Nevertheless, wall tangent computation with a 9×9 pixel block provides a consistent angle estimation on both of the bifurcation models. In this work, a 9×9 pixel block was used for the sliding neighborhood operation to estimate the tangent vectors. In general, a larger block would give a better angle estimate, but it would also increase the chances of capturing unwanted features into the block. For example, in the 50% stenosed bifurcation model, a large pixel block (e.g., 15×15) will capture both the upper and lower wall at the site of the stenosis. By *ad-hoc* evaluation, a 9×9 block is an optimal choice.

## 4.3 Regularization of Velocity Profiles

Fig. 4.3 shows the results of the velocity profile reconstruction using the DCT-based penalized regression method, which has been described in Subsection 3.2.2. The dashed lines represent the original velocity profiles which were constructed using $\tilde{v} = 1 - \left|\frac{r}{R}\right|^n$, as in formula (3-13). The valid data (circle markers) represent the velocity profiles with the velocities lower than the thresholds removed. The velocities at the wall positions were kept at zero as the no-slip condition were applied. The red curves represent the reconstructed profiles. Results indicate that the

reconstructed profiles show close agreement with original profiles when the threshold is below 50% of the maximum velocity. When a threshold 0.7 is used, the reconstructed profiles start to slightly deviate from the original ones. As illustrated in the RMSE graph (Fig. 4.4), the estimation errors range from 0.5% to 2.5% overall. From the graph, it can be seen that the estimation errors go up when a higher threshold value is used. The RMSE increases by approximately 3 times between threshold value $0.1v_{norm}$ and $0.7\ v_{norm}$. Also, Fig. 4.4 points out that the degree of flattening of the profile (i.e., *n*) does not has a significant influence on the estimation error.

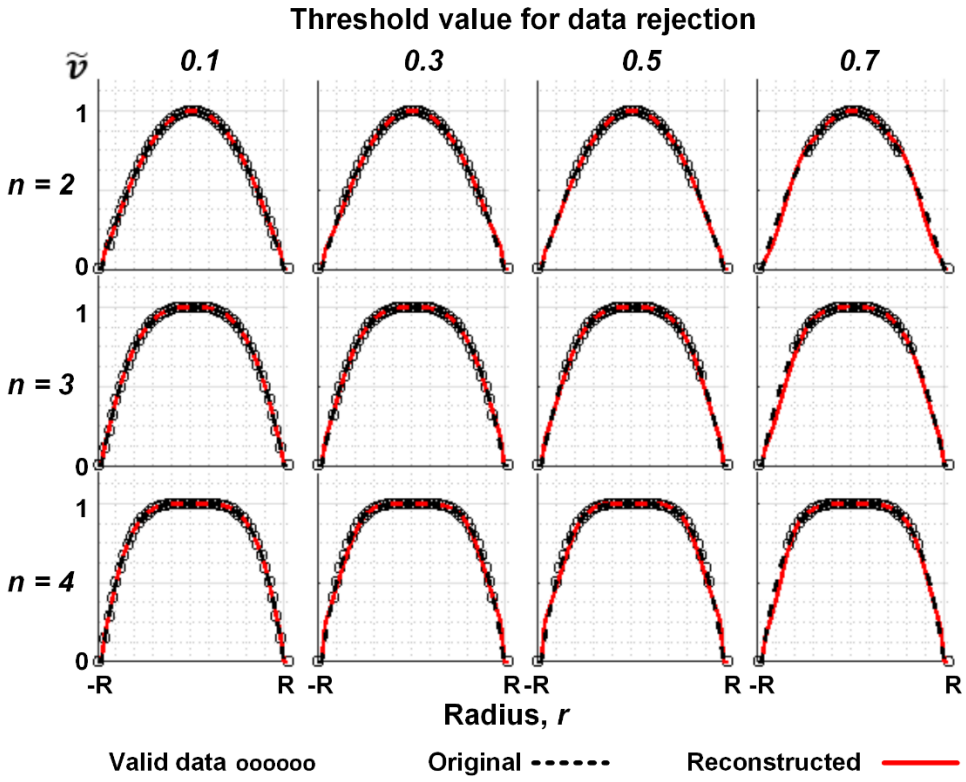


Fig. 4.3. Comparison between the reconstructed velocity profiles and the original profiles (constructed based on $\tilde{v} = 1\text{-}|r/R|^n$ where *n* ranges in 2 to 4). The valid data represent the velocity profiles with the velocity data below the threshold values (0.1, 0.3, 0.5, or 0.7) removed.

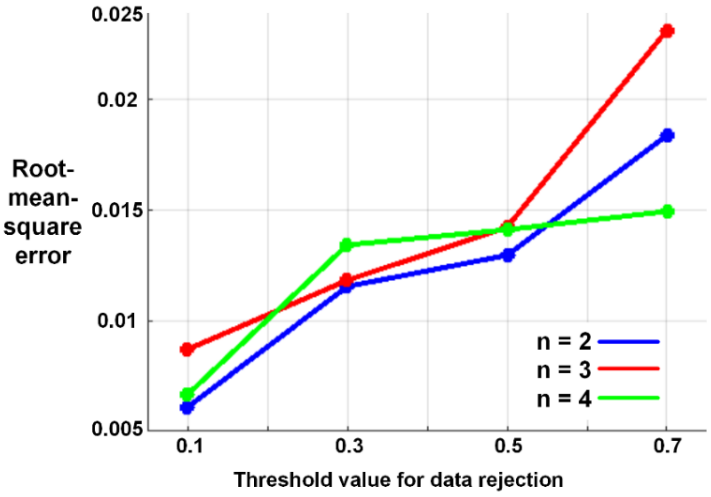


Fig. 4.4. Effect of the threshold value toward the velocity profile reconstruction error.

## 4.4 Performance Investigations of Wall Shear Rate Estimation

### 4.4.1 Accuracy of Wall Shear Rate Estimation

The flow vector maps generated using the high-frame-rate multi-angle Doppler method are shown in Fig. 4.5a-c (top row). The magnitudes of the flow velocities are indicated by the colour and length of the arrows, and the flow directions are equivalent to the pointing directions of the arrows. It can be seen that the flow profiles in all three different flow rate setups are approximately parabolic in general. The flow velocities decrease along the length of the flow channel (from left to right). The peak velocities (centerline) across the imaging view drop from 40.1 cm/s to 27.8 cm/s, 25.1 cm/s to 16.9 cm/s, and 12.2 cm/s to 8.4 cm/s for 4.5 mL/s, 3.0 mL/s, and 1.5 mL/s setup respectively.

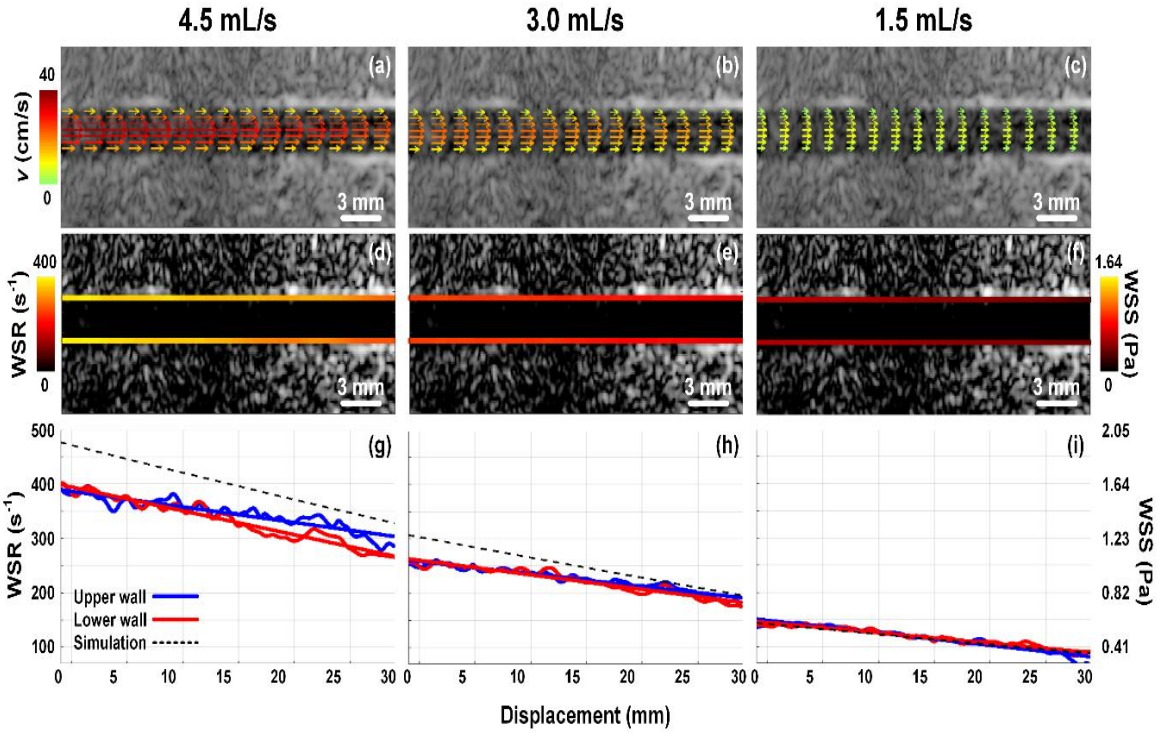


Fig. 4.5. Imaging experiments upon the Hele-Shaw flow chamber under a steady flow at 4.5 mL/s, 3.0 mL/s, and 1.5 mL/s flow rates. (a) Flow vectors acquired using the multi-angle Doppler approach. The flow velocities are displayed in colour-encoded arrows overlaying onto the B-mode images. (b) WSR maps obtained using the WSR estimation algorithm. The WSR levels at the detected wall positions overlay onto the B-mode images. (c) WSR values on the upper and lower walls of the flow channels, and the reference WSR values obtained from CFD simulations.

The second row (Fig. 4.5d-f) depicts the WSR distribution along the detected wall positions. Similar to the vector maps, the colours indicate the magnitude of the WSR. Given the characterized dynamic of the BMF viscosity ($\mu$ = 0.0041 Pa·s), the corresponding WSS values are also calculated according to the equation (2-12). Qualitatively, the decreasing trend of the WSR levels along the length of the flow channel can be observed as the colours are brighter at the inlet and dimmer at the outlet. The quantitative comparison of the WSR patterns to the CFD simulation results is shown in Fig. 4.5g-i (bottom row). The WSR computed from CFD simulation (dashed line), and the WSR of the upper wall (blue curve) and the lower wall (red curve) along the length of the channel are plotted. The corresponding linear regression lines for the estimated WSR are also shown in the same graph.

Table 4.1 provides the slopes and intercepts of these lines, the linearity of the regression line in terms of correlation coefficient, as well as the percentage drops in the WSR levels across the imaging view (i.e., displacement = 0 to 30 mm).

| Flow rate | | Slope ($s^{-1}mm^{-1}$) | Intercept ($s^{-1}$) | Pearson correlation coefficient | Percentage drop of WSR across the imaging view |
|---|---|---|---|---|---|
| **4.5 mL/s** | Simulation | -4.77 ± 0.00 | 492.90 ± 0.00 | 0.998 | 29% |
| | Upper wall | -2.85 ± 0.14 | 400.44 ± 2.90 | 0.968 | 21% |
| | Lower wall | -4.38 ± 0.12 | 416.13 ± 2.42 | 0.971 | 31% |
| **3.0 mL/s** | Simulation | -3.59 ± 0.00 | 320.09 ± 0.00 | 0.999 | 34% |
| | Upper wall | -2.29 ± 0.07 | 269.85 ± 1.55 | 0.962 | 25% |
| | Lower wall | -2.66 ± 0.09 | 273.80 ± 1.80 | 0.961 | 29% |
| **1.5 mL/s** | Simulation | -1.79 ± 0.00 | 150.00 ± 0.00 | 0.999 | 36% |
| | Upper wall | -2.29 ± 0.07 | 160.24 ± 1.41 | 0.919 | 43% |
| | Lower wall | -1.89 ± 0.05 | 154.30 ± 1.09 | 0.974 | 36% |

Table 4.1. The slopes and intercepts of the regression lines shown in Fig. 4.5g-i, and the percentage drops in the WSR levels across the imaging view.

Fig. 4.2g-i indicate that the estimated WSR patterns along both upper and lower walls show similar decreasing trends as compared to those obtained from CFD simulations. This trend can also be seen in the rightmost column of Table 4.1, which reveals that the maximum difference of the WSR percentage drop between the measurement and simulation is 10%. Also, the linearity of the WSR drop along the length of the channel can be observed as the plots shown only slight deviations between the estimated WSR and the regression lines, and their correlation coefficients were greater than 0.9. From Fig. 4.2g-h, an underestimation of the WSR levels is observed, and the bias is more prominent in the high WSR regions. The reason for this deviation will be discussed in Subsection 5.2.3. Overall, the proposed WSR estimation is able to resolve the linearly decreasing WSR patterns in the Hele-Shaw flow chamber. As well, the estimated WSR values are comparable to those obtained from CFD simulations.

### 4.4.2 Sensitivity to Wall Positions

The WSR estimation error as a function of the wall position estimation error (within ± 10%) is reported in Fig. 4.6. The detected wall positions used in the previous experiment are used as the reference positions. As a flow channel with 3 mm gap was used in this study, every 3.3% of wall position error refers to a 0.1 mm shift. A negative wall position error represents that the wall position is further away from the centre of the flow channel. Similarly, a positive wall position error indicates that the wall position is localized closer to the centre of the flow channel. Results show that the WSR are underestimated when the wall positions are incorrectly localized inside the tissue region, and WSR are overestimated when the wall positions are located within the flow region. Every 3.3% wall position error produces roughly 10% error in the WSR estimation. Also, results show that the wall position estimation error produces no significant difference between the WSR estimation on the upper wall and lower wall.

In practice, the vessel walls are not stationary but pulsating due to the pulsatile blood flow. According to Hansen, Mangell, Sonesson, and Lanne (1995), the representative distension in a carotid artery of a 60-year-old human is about 6%. Therefore, with the fixed wall positions used in this study, the WSR estimation would produce approximately 18% error. To refine the current estimation method, a dynamic wall tracking algorithm would be needed. More details will be discussed in Subsection 5.3.3 and 5.4.1. On the other hand, subject movements may cause a shift of the vessel wall positions in the imaging view. However, in clinical practice, the subject is often asked to hold their breath during the imaging duration (1 s for the proposed imaging protocol). As such, the subject movement within a short time window should be negligible.

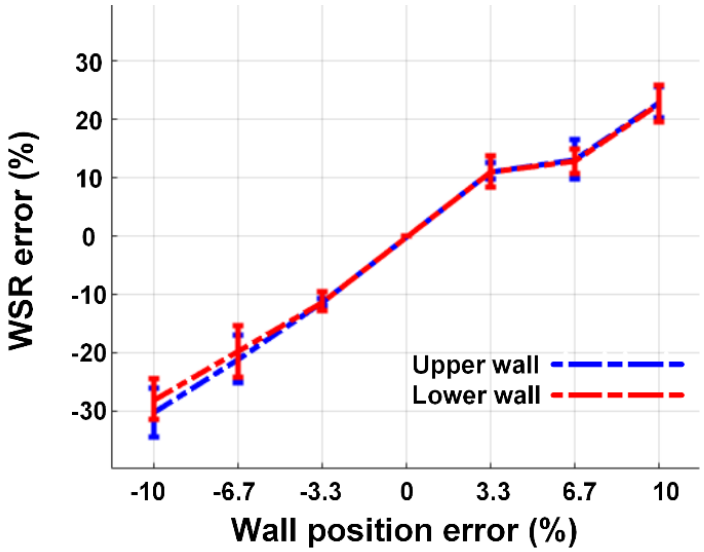


Fig. 4.6. WSR estimation error results from the wall position error.

## 4.5 Spatiotemporal Wall Shear Rate Mapping: *In Vitro* Study

### 4.5.1 Healthy carotid bifurcation model

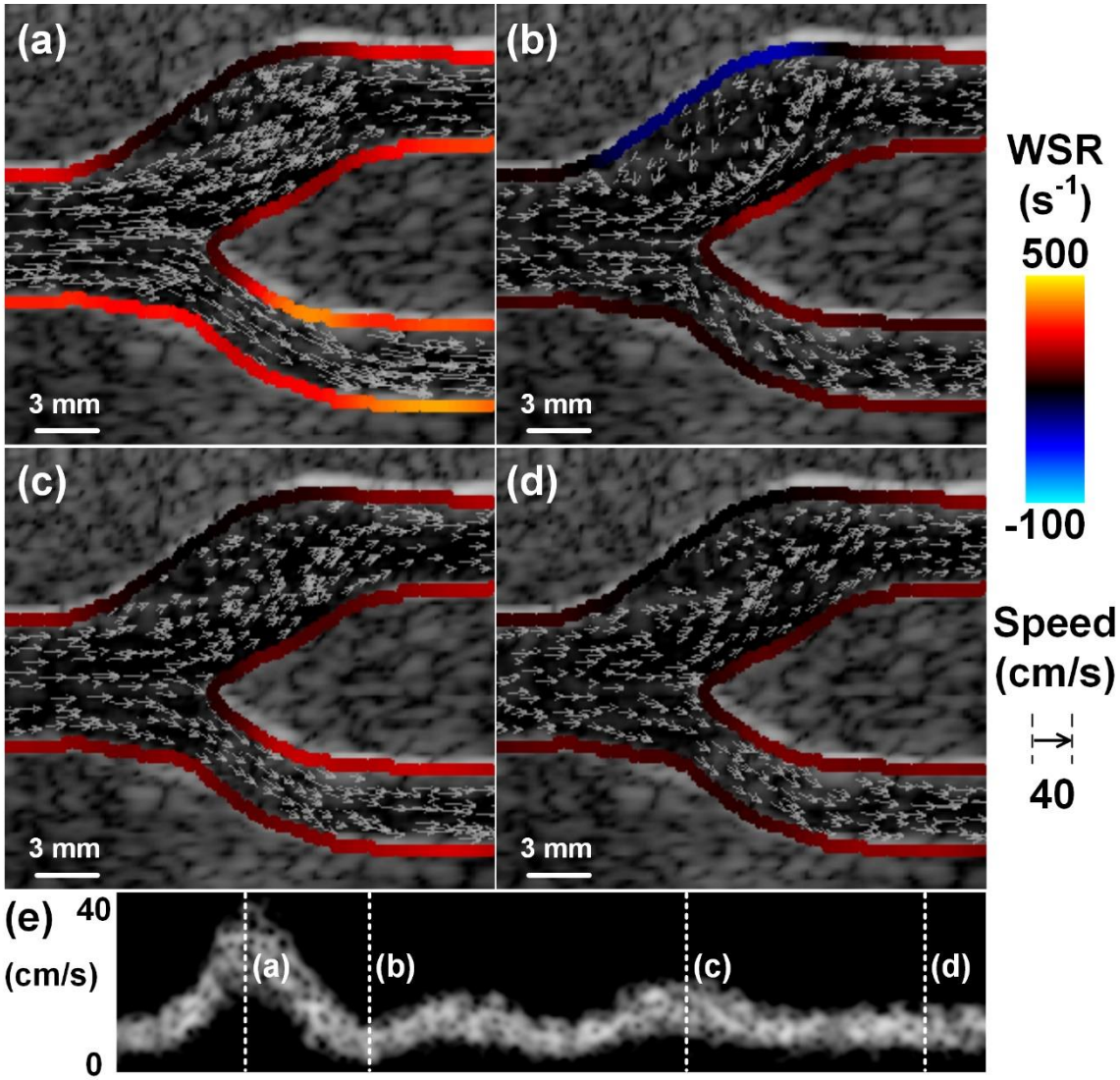


Fig. 4.7. Spatiotemporal WSR maps of the healthy carotid bifurcation flow phantom under a pulsatile flow (peak flow rate: 8.0 mL/s). Four representative phases are shown: (a) peak systole, (b) post-systolic phase, (c) dicrotic wave peak, and (d) diastole. (e) Doppler spectrogram acquired at the centre of the CCA branch inlet.

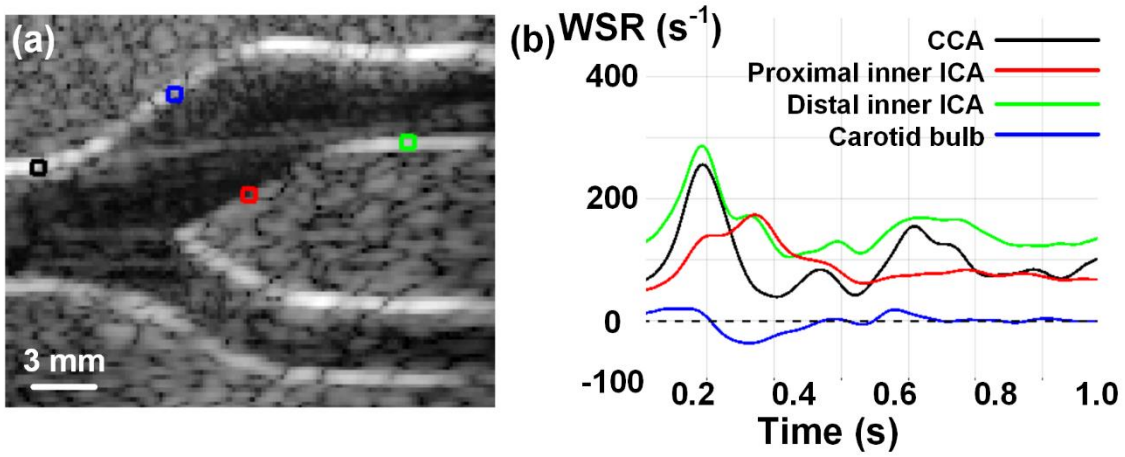


Fig. 4.8. WSR measured at selected positions of the healthy carotid bifurcation phantom. (a) The selected measurement positions at CCA, the inner wall of proximal ICA, the inner wall of distal ICA, and carotid bulb region are overlaying upon the B-mode image. (b) A plot of the temporally varying WSR levels at the selected positions.

***Spatiotemporal wall shear rate map***

Using the proposed WSR estimation technique, a time-resolved quantification of the WSR dynamics in anthropomorphic phantoms under a pulsatile flow is achieved. Movie 1 (Appendix A) shows a cine loop of the long-axis view of the flow dynamics and WSR distribution inside the healthy carotid bifurcation model. Four representative frames are shown in Fig. 4.7. The selected key time-points are peak systole (Fig. 4.7a), post-systolic phase (Fig. 4.7b), dicrotic wave peak (Fig. 4.7c), and diastole (Fig. 4.7d). The vector maps are also displayed to indicate the flow velocities and directions. The lengths of the arrows represent the magnitude of the velocity vectors. Single colour display for the vectors is used here to highlight the WSR maps. Fig. 4.7e shows the Doppler spectrogram at the CCA branch, which is the flow inlet. The data acquisition rate $f_{DAQ}$ was 3.3 kHz, and the nominal frame rate of the vector estimation was 416 kHz. In general, the WSR patterns are found to be synchronized with the stroke of the flow pulse. At the CCA, ECA, and the inner wall of the ICA sinus, the WSR levels reached their local maxima during the peak systole and fell rapidly after the systolic phase. Then the dicrotic wave brought the WSR at the CCA and distal ICA to the second highest

levels. Finally, The WSR levels remained relatively low during the diastolic phase. The evolution of the WSR patterns throughout the entire cycle was quantitatively presented in Fig. 4.8.

***Influence of vascular curvature on wall shear rate***

Using the proposed WSR estimation method, the variation in the WSR levels due to the curvature of vascular geometries can be observed. This effect is most significant in the systolic phase. Fig. 4.7a shows that the positions of the peak WSR level on the inner and outer wall of the ECA branch are different. For the inner ECA wall, the WSR level at the proximal end (closer to the bifurcation point) was higher than that at the distal end (closer to the flow outlet). In contrast, for the outer ECA wall, the WSR level at the proximal end was lower than that at the distal end. This difference in the WSR between the inner and outer walls was associated with the bending of the ECA. At the bending point, a centripetal force was generated to force the fluid to change its main flow direction. The force acted uniformly over the cross-section of the lumen. However, the faster-moving fluid was less sensitive to the force than the slower-moving fluid because of their greater inertia. As a result, the faster-moving fluid was swept out towards the outer ECA wall, and the slower moving fluid occupied the inner wall. Hence, the velocity profile over the cross-section at the bend was distorted, with a higher velocity gradient at the outer ECA wall.

***Negative wall shear rate due to flow recirculation***

The WSR levels found in the vessel walls in CCA branch, ECA branch, and the inner wall of ICA branch are positive throughout the entire pulse cycle. In contrast, it can be seen that the outer wall of ICA (where the carotid bulb is located) exhibits a negative WSR level during the post-systolic phase (Fig. 4.7b). Also, from Fig 4.8b, it can be observed that (i) the WSR level at the carotid bulb region changed from positive to negative after the systole, and (ii) the average WSR level was close to zero at this region. It is because a flow recirculation zone was developed within the ICA sinus. Two contributing factors were leading to the development of the flow recirculation: (i) flow channel expansion due to the enlarged carotid bulb region, and (ii) the curved path for the fluid moving from

CCA to ICA. A vortex was created in the bulb region, and it can be visualized by the vector map where the arrows are pointing in the opposite direction to those at the inlet. The vortex then dissipated when the dicrotic wave arrived and produced a secondary flow upstroke (Fig, 4.6c). The flow in the carotid bulb returns to a forward flow after this point.

### 4.5.2 Stenosed carotid bifurcation model

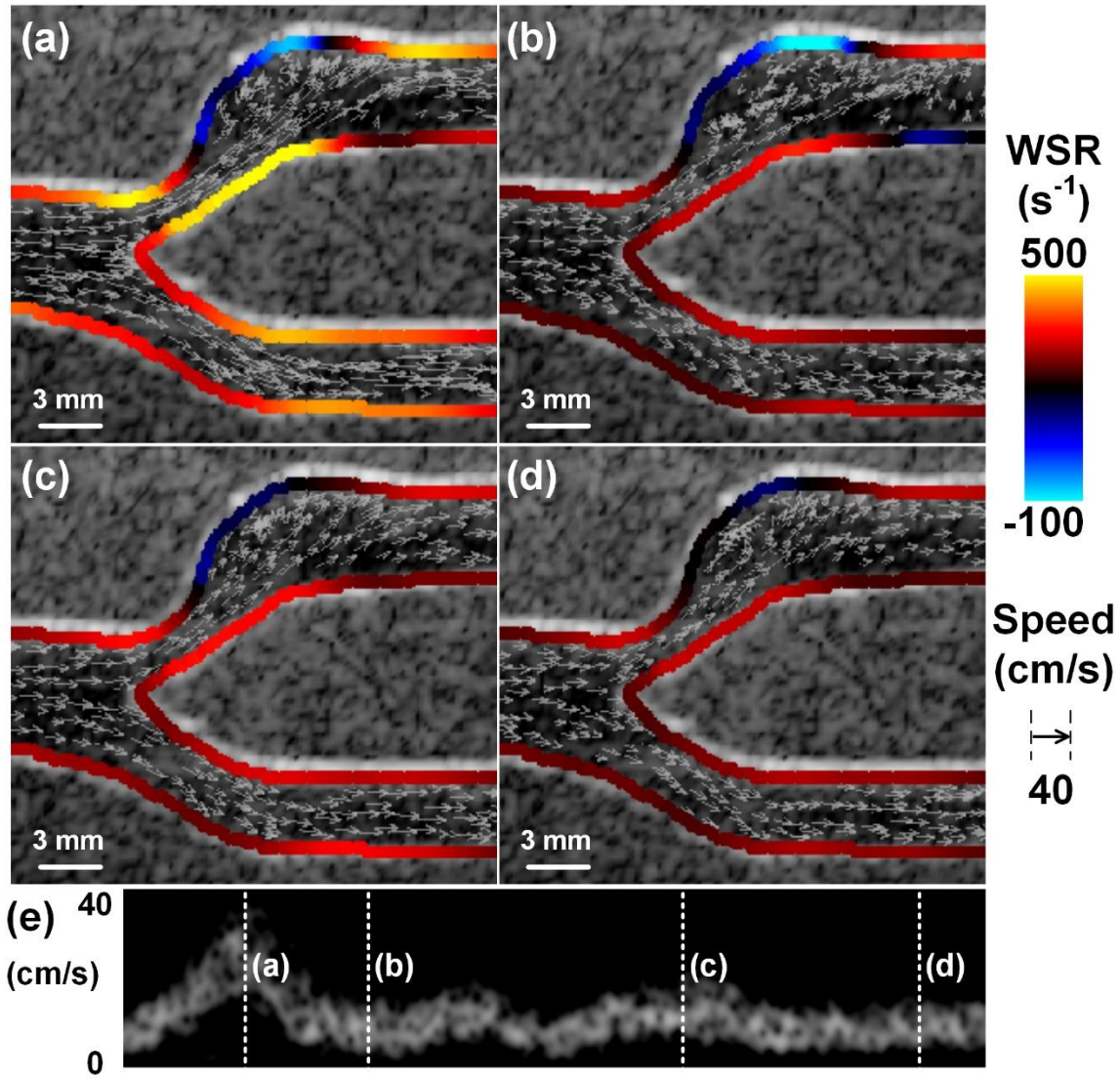


Fig. 4.9. Spatiotemporal WSR maps of the diseased carotid bifurcation flow phantom (50% eccentric stenosis) under a pulsatile flow (peak flow rate: 8.0 mL/s). Four representative phases are shown: (a) peak systole, (b) post-systolic phase, (c) dicrotic wave peak, and (d) diastole. (e) Doppler spectrogram acquired at the centre of the CCA branch inlet.

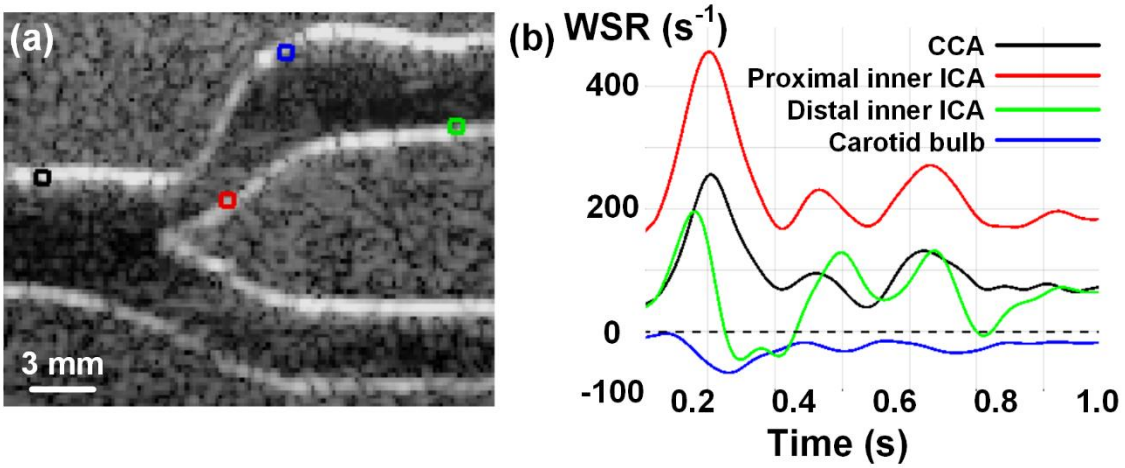


Fig. 4.10. WSR measured at selected positions of the stenosed carotid bifurcation phantom. (a) The selected measurement positions at CCA, the inner wall of proximal ICA, the inner wall of distal ICA, and carotid bulb region are overlaying upon the B-mode image. (b) A plot of the temporally varying WSR levels at the selected positions.

***Effect of flow jets on wall shear rate***

A cine loop of the flow dynamics and WSR distribution inside the carotid bifurcation model with 50% eccentric stenosis is shown in Movie 2 (see Appendix B). In this diseased model, a flow jet was formed at the stenosed region, i.e., the entrance to the ICA branch. The vessel walls at this region experienced a strong shearing force due to the accelerated flow, which resulted from the vessel narrowing (see Fig. 4.9a). This high WSR region can be found at the entrance of the ICA and propagate along the proximal ICA inner wall. Fig. 4.10b highlights the elevated WSR level at the entrance of the ICA. The WSR level at the ICA entrance almost doubled that at the CCA. The flow jet then collided with the outer ICA wall near its distal end. This collision led to an elevated WSR level at the distal end of the ICA outer wall as well.

***Amplified flow reversal and reattachment point***

The WSR maps of the stenosed bifurcation model during peak systole (Fig. 4.9a) indicates a more negative WSR level in the carotid bulb region as compared to the findings in the healthy model. This observation is associated with the amplified flow recirculation at the bulb region. The stenosis

was more severe in this model so that a stronger adverse (more positive) pressure gradient developed. This opposing force to the fluid led to a more pronounced flow recirculation. Also, 4.10b reveals that the WSR level at this region remained negative throughout the entire cycle. This observation is because the vortex was sustained at that region without dissolution, as illustrated by the vector maps Fig. 4.9a-d. After the termination of the recirculating flow, the flow became reattached to the straight outer-wall region at the distal ICA. The reattachment point, which had a zero WSR, can be found at the transition region between the negative (proximal outer wall) and positive (distal outer wall) WSR region. During post-systolic phase (Fig. 4.9b), it can be observed that the reattachment point slightly moved towards the distal end of the ICA branch (approximately 2 mm).

***Second recirculation zone***

Another distinct feature observed in the diseased bifurcation model is the negative WSR region at the distal end of the ICA inner wall. In fact, this is the second recirculation zone which emerged only during the post-systolic phase (see Fig. 4.9b). This recirculation zone formed after the flow jet front had completed its propagation from the narrowed site to the ICA outer wall. Subsequently, the slow-flow components circulated on the inner wall side. This recirculation zone was weaker the one at the carotid bulb region, so the WSR level was lower in magnitude (as shown in Fig. 4.10b). After that, vortex shedding took place, so the recirculation disappeared. During the dicrotic wave peak, the WSR level barely reached zero from the positive side, without going any further into the negative side. It is because the flow jet formed during the dicrotic wave peak was not as strong as the one formed during peak systole. Therefore, the recirculation was less significant at the inner wall segment.

# CHAPTER 5

# Significance of Study Findings and Conclusions

## 5.1 Summary of Contributions

Using ultrasound imaging technique to quantify WSR patterns in complex flow dynamics is not a trivial task. The WSR patterns are spatially and temporally varying in the human vasculature (e.g., carotid bifurcation) because of two factors: (i) the tortuous nature of vascular geometries; (ii) pulsatile behaviour of the flow pulse. To measure the WSR under these conditions, we have developed a new WSR imaging tool to monitor such spatiotemporally changing WSR dynamics.

One of the major challenges in WSR estimation is that the near-wall velocity estimates are often affected by clutter filtering. A DCT-based penalized least-squares regression method has been adapted to regularize the velocity profiles so that more accurate and consistent near-wall velocity gradients can be obtained. The velocity gradient maps are computed using Sobel filter which is composed of a central difference kernel and a smoothing kernel. The smoothing kernel further reduces the effect of random noises that may present in the velocity estimates. Also, to extract the tangential components of the velocity gradients, 2-D coordinate transformations have been implemented to the detected wall positions on the gradient maps. This procedure is realized by first computing the wall tangent vectors using a sliding pixel block to determine the second moment within the block. By finding the ellipse with the equivalent second moment, the orientation of the ellipse can be used to represent the wall orientation.

Two phantom studies have been carried out to evaluate the performance of the WSR estimation. The first one involves the use of a Hele-Shaw flow chamber that can generate a linear wall shear rate field. This experimental setup has well-characterized geometries and flow conditions.

Therefore, it can act as a calibration tool for evaluating the estimation accuracy and quantifying the wall position errors. The second study consists of two anthropomorphic flow phantoms: a healthy carotid bifurcation and a diseased carotid bifurcation with 50% eccentric stenosis. These anatomically realistic models mimic the complex flow dynamics in human arteries so that WSR patterns detected in these phantom models would be relevant to *in-vivo* conditions. It is worth mentioning that the phantom models were built based on 3-D printing technology, which allows the models to be designed and constructed in arbitrary geometries (Ho et al., 2017).

## 5.2 Significance of Study Findings

### 5.2.1 Computation of Tangent Vectors at Wall Positions

Determining the tangential directions at the wall positions is an important part of the WSR estimation algorithm since WSR is represented by the tangential velocity gradient at the wall position. The tangential directions along the vessel wall have to be determined, and the computed angles will be used in the coordinate transformation in the later stage. Hence, the accuracy of the wall tangent estimation would ensure accurate WSR estimates. The validation study shows that the wall orientation computation algorithm gives an accurate estimation of the tangent vectors. The applicability of the algorithm is also demonstrated in the carotid bifurcation models. Results show that the algorithm works well on carotid bifurcation geometries.

The estimation accuracy is associated with the choice of size of the search block. Although the relationship is not extensively studied in this work, the accuracy is expected to be higher when a larger block size is used. However, the trade-off is that finer features in the image may hamper the tangent computation since they introduce some unwanted, weighted pixels into the calculation of second moments. A 9×9 block used in this work works well in computing the wall orientation of the bifurcation models. However, if the models exhibit smaller features or highly tortuous vascular

geometry (e.g., cerebral arteries), a smaller block might be more suitable. The visualizations in Fig. 4.2 can be leveraged to facilitate the selection of block size.

### 5.2.2 Regularization of Velocity Profiles

In assessing the velocity profile, parabolic profiles (Carallo et al., 2006; Cho et al., 2016) and Womersley flow (Blake, Meagher, Fraser, Easson, & Hoskins, 2008) are the most typical approaches. However, the use of mathematical models is highly idealized since their straight tube assumption is hardly valid in human vascular geometry. In addition, the flow profiles in complex flow dynamics might not be well-defined using a low-order polynomial. On the other hand, the velocity measurement is affected by the clutter filtering that is used to reject the clutter noise produced by the vessel wall. In this work, the velocity profiles are simultaneously smoothed and interpolated using a DCT-based penalized regression (Garcia, 2010), which is known as a regularization approach. As seen in Fig.4.3, this algorithm is able to recover the velocity profiles when the near-wall velocity estimates are removed. From the validation study, the reconstructed profiles produce very small estimation errors as compared to the ideal profiles. A feature of this method is that it does not rely on any presumption for the velocity profiles. Hence, it is expected that this method would be applicable in measuring the velocity profiles in complex flow dynamics because the profiles usually cannot be defined in a simple way.

### 5.2.3 Evaluation of Wall Shear Rate Estimation Accuracy

The WSR estimation accuracy is evaluated using a Hele-Shaw flow chamber with a known, linearly decreasing WSR field. This design has been applied to evaluate the WSR estimation performance over several cross-sectional planes (Tsou et al., 2008). However, this measurement method requires repositioning the ultrasound transducer, hence possibly introducing other experimental errors. More importantly, the sensitivity of the WSR estimation over a small region (within an imaging view) cannot be assessed. To our knowledge, this work is the first application of

this flow chamber for assessment of WSR estimation accuracy within an imaging view, which is scanned over the longitudinal plane of the flow chamber. Results (Fig. 4.5) indicate that the WSR estimation method is capable of detecting the linearly decreasing trend of WSR (~30% drop) within a 30 mm imaging view in all three flow rate setups. It is worth noting that the WSS fields produced by the three setups cover the atherogenic (< 0.4 Pa) and atheroprotective (> 1.2Pa) shear ranges (Malek et al., 1999). Plaque formation is favored in the atherogenic region, while the atheroprotective region keeps the vessel wall healthy (Malek et al., 1999; Kornet, Lambregts, Hoeks, & Reneman, 1998). It indicates that the proposed method has the potential to detect abnormal WSR levels which could be beneficial to early diagnosis for atherosclerosis before stenosis occurs.

The current WSR estimation may give rise to underestimation bias, as seen in Fig. 4.5h-i. This issue is probably due to two factors. First, since unfocused plane wave transmission was used to acquire high-frame-rate data, the corresponding point spread function was less sharp (i.e., a wider main lobe) than that produced using conventional scanline-based ultrasound imaging (Holfort, Gran, & Jensen, 2009). Therefore, some unwanted slow-flow components outside the nominal pixel boundaries would also be captured (Yiu & Yu, 2016). As a result, the velocities would be underestimated, and the error would be directly translated to WSR underestimation bias. Second, the velocity estimation is based on lag-one autocorrelation, which is a mean Doppler frequency estimation. The resulting velocity estimate at given pixel position was an average of all the velocity components. Hence, the averaging effect would be more significant when there is a rapid change in flow velocity. It explains why the WSR underestimation bias is larger in the higher WSR region (i.e., closer to the inlet).

### 5.2.4 Performance study on anthropomorphic flow phantoms

The capability of the proposed WSR estimation method to quantify the spatiotemporally varying WSR is demonstrated in physiologically relevant geometries. For the healthy carotid bifurcation model, a transient presence of the flow recirculation zone is detected in the carotid bulb

region (Fig. 4.7b). The flow recirculation is known to be associated with the branching angle and the diameter of the ICA branch (Hobson, Wilson, & Veith, 2005). In this region, the average WSR level is close to zero over the entire cycle. Similar observations have been reported in other studies (Ku et al., 1985; Resnick et al., 2003). As suggested by Koskinas et al. (2009), this low and oscillatory WSS level is likely associated with the formation of rupture-prone plaques. This finding suggests that the proposed WSR estimation method might potentially be used in predicting the risk of plaque development.

More complex WSR dynamics can be observed in the stenosed carotid bifurcation model, which represents a diseased state of the artery. The narrowed ICA entrance represents the place where the plaque is located. From Fig. 4.9, it can be observed that this region exhibits a significantly higher WSR level than other parts. As reported by Groen et al. (2008), the strong shear forces may pose an elevated risk of plaque rupture. In turn, there would be a higher chance of triggering a stroke. Another distinct feature of the WSR pattern found in the diseased model is the presence of the second recirculation zone at the distal end of the inner ICA wall. It leads to an oscillatory WSR level at this region. These findings suggest that the WSR estimation might be used to differentiate WSR patterns between the healthy and diseased states of carotid arteries. In addition, the WSR patterns observed in this study match well with those measured using optical PIV method (Kefayati et al., 2014) and contrast-based ultrasound imaging (Leow & Tang, 2018).

## 5.3 Advantages and Limitations of Proposed Method

### 5.3.1 High-frame-rate Spatiotemporal Mapping of Wall Shear Rate

Plane-wave transmission technique enables a high-frame-rate ultrasound data acquisition without losing the spatial dimension. It facilitates the assessment of the spatially varying WSR dynamics within an imaging view. It can provide more intuitive information as compared to the spectral-Doppler-based approach which estimates the WSR at the wall positions lying on a single

beamline (Ricci, Swillens, Ramalli, Segers, & Tortoli, 2017). Also, the high temporal resolution is essential to track the temporally varying flow dynamics in the human blood flow. Meanwhile, the multi-angle Doppler approach allows the flow velocities to be determined without angle ambiguity, which is recognized as a major issue in conventional CFI-based methods (Evans, 2010). With these two features, the high-frame-rate WSR spatiotemporal mapping would facilitate the quantification and visualization of the WSR distribution in complex flow dynamics.

### 5.3.2 Sobel Operator for Velocity Gradient Estimation

Earlier efforts on WSR estimation are mostly based on computing the near-wall velocity gradient along a one-dimensional line across the vessel lumen (Blake et al., 2008; Leow & Tang, 2018; Ricci et al., 2017). These methods, however, might be more sensitive to the random noise present in the velocity estimates. In this work, Sobel kernels were used to estimate the velocity gradients from the vector map. There are two main advantages of using this approach. First, since the Sobel kernels include an averaging filter, it provides a smoothing effect which can reduce the influence of the random noise of the image. Hence, it allows a more consistent velocity gradient estimation. Second, a 2-D filter is relatively easy to implement on the vector maps which are pixel maps. It reduces the computation cost of the WSR estimation algorithm, thereby offering a shorter data processing time.

### 5.3.3 Detection of Wall positions

A rigid wall assumption has been made in this work. It means that the vessel walls are assumed stationary. This assumption is valid within the scope of this study because the PVA-based tissue mimic has a relatively high elastic modulus (> 100 kPa). The wall motion caused by the fluid flow is less than 1% in all phantom models with the current flow setups. According to Fig. 4.6, this magnitude of the wall motion would give rise to approximately 3% WSR estimation error. However, in *in-vivo* conditions, arterial wall motion is often more significant. As reported in an *in vivo* study

(Golemati et al., 2003), the average wall displacement in the carotid artery is about 0.3 mm, which can be translated into about 10% change in wall positions in our phantom setup. If the estimated wall position remains unchanged while there are significant axial movements of the artery wall, it is expected that the WSR would be underestimated. To address this issue, updating the wall positions for each data frame is essential in order to improve the WSR estimation accuracy. Some possible solutions will be discussed in the Subsection 5.4.1.

## 5.4 Future Directions

### 5.4.1 Dynamic Wall Tracking Algorithm

To accurately measure the WSR in elastic and pulsating arteries, it is necessary to implement a wall tracking algorithm that can dynamically detect the wall positions. A few active-contours based solutions have been proposed. For example, Gemignani, Paterni, Benassi, and Demi (2004) suggested a robust contour tracking technique that exploits an edge detector algorithm. The edge detector was obtained by the generalization of the first order absolute central moment operator. The applicability of this method has been demonstrated in tracking the wall positions in carotid bifurcations (Ricci et al., 2017). A localized region-based active contour segmentation method has been reported by Lankton and Tannenbaum (2008). This algorithm is based on minimizing the energy of a local region in a B-mode image to evolve a contour for wall segmentation. It is proved that this method can provide an accurate segmentation for heterogeneous objects such as medical images.

In the current framework, the B-mode images are acquired at high temporal resolution (3.3 kHz). Implementing an automated wall tracking algorithm to our framework will allow a time-resolved quantification of wall movements under pulsatile flow conditions in arteries. It is expected that the accuracy of the WSR estimation in *in-vivo* setting can be improved by dynamically updating the wall positions.

### 5.4.2 Role of Hemodynamic Wall Shear Rate in Other Arteries

Apart from predicting the plaque formation and its rupture risk in carotid arteries, the WSR imaging could potentially be applied to other human arteries. For example, the WSR level in brachial arteries contributes to the production of vasoactive mediators, such as nitric oxide which regulates the vasodilation (i.e., dilation of arteries) to increase blood flow (Koller & Kaley, 1995). This brachial artery flow-mediated dilation is associated with the endothelial health and function. Therefore, brachial WSR could be an indicator of vascular diseases and a potential marker of cardiovascular risk (Bots, Westerink, Rabelink, & Koning, 2004). On the other hand, the WSS in cerebral arteries is also related to the occurrence of cerebral aneurysms (Nixon, Gunel, & Sumpio, 2010). Studies have shown that the cerebral bifurcation points (apices) are the most common sites of aneurysm formation (Horikoshi, Akiyama, Yamagata, Sugita, & Nukui, 2002; Ingebrigtsen et al., 2004; Atlas, 1997). It is worth mentioning that the phantom fabrication protocol used in this work can be directly adopted to construct anatomically realistic phantom models. The phantom models will facilitate the studies of WSR measurements in brachial and cerebral arteries.

## 5.5 Research Summary

WSR is known to be strongly associated with stroke-related conditions, such as carotid plaque development and its rupture-risk. In this thesis, an ultrasound-based WSR quantification technique has been developed to seek to provide a non-invasive stroke risk evaluation method. The WSR imaging method is built based on four key principles: 1) high-frame-rate-vector estimation, 2) regularization of the velocity profiles, 3) velocity gradients mapping using Sobel filters, and 4) tangential velocity gradient computation. A Hele-Shaw flow chamber with a linear WSR field is designed to evaluate the WSR estimation accuracy. Results indicate that the proposed method can detect the spatially varying WSR pattern and provide accurate estimates in the low WSR region. *In vitro* experiments using two anthropomorphic flow phantoms: healthy and diseased carotid

bifurcations are carried out to demonstrate the capability of the proposed method in quantifying and visualizing the spatiotemporally changing WSR distributions in complex flow dynamics. This WSR estimation technique can offer both spatial dimension (entire imaging view) and adequate temporal resolution (data acquisition at 0.3 ms) that the conventional methods such as CFD and spectral Doppler cannot provide.

# References


Atlas, S. W. (1997). Magnetic resonance imaging of intracranial aneurysms. Neuroimaging clinics of North America, 7(4), 709-720.

Azran, A., Hirao, Y., Kinouchi, Y., Yamaguchi, H., & Yoshizaki, K. (2004). Variations of the Maximum Blood Flow Velocity in the Carotid, Brachial and Femoral Arteries in a Passive Postural Changes by a Doppler Ultrasound Method. *The 26th Annual International Conference of the IEEE Engineering in Medicine and Biology Society*. doi:10.1109/iembs.2004.1404041

Bercoff, J., Montaldo, G., Loupas, T., Savery, D., Mézière, F., Fink, M., & Tanter, M. (2011). Ultrafast compound doppler imaging: Providing full blood flow characterization. *IEEE Transactions on Ultrasonics, Ferroelectrics and Frequency Control, 58*(1), 134-147. doi:10.1109/tuffc.2011.1780

Birchall, D., Zaman, A., Hacker, J., Davies, G., & Mendelow, D. (2006). Analysis of haemodynamic disturbance in the atherosclerotic carotid artery using computational fluid dynamics. *European Radiology, 16*(5), 1074-1083. doi:10.1007/s00330-005-0048-6

Blake, J. R., Meagher, S., Fraser, K. H., Easson, W. J., & Hoskins, P. R. (2008). A Method to Estimate Wall Shear Rate with a Clinical Ultrasound Scanner. *Ultrasound in Medicine & Biology, 34*(5), 760-774. doi:10.1016/j.ultrasmedbio.2007.11.003

Bots, M. L., Westerink, J., Rabelink, T. J., & Koning, E. J. (2004). Assessment of flow-mediated vasodilatation (FMD) of the brachial artery: Effects of technical aspects of the FMD measurement on the FMD response. *European Heart Journal, 26*(4), 363-368. doi:10.1093/eurheartj/ehi017

Brech, R., & Bellhouse, B. J. (1973). Flow in branching vessels. *Cardiovascular Research, 7*(5), 593-600. doi:10.1093/cvr/7.5.593

Browne, J. E. (2014). A review of Doppler ultrasound quality assurance protocols and test devices. *Physica Medica, 30*(7), 742-751. doi:10.1016/j.ejmp.2014.08.003

Burckhardt, C., Grandchamp, P., & Hoffmann, H. (1974). An Experimental 2 MHz Synthetic Aperture Sonar System Intended for Medical Use. *IEEE Transactions on Sonics and Ultrasonics, 21*(1), 1-6. doi:10.1109/t-su.1974.29783

Burlew, M. M., Madsen, E. L., Zagzebski, J. A., Banjavic, R. A., & Sum, S. W. (1980). A new ultrasound tissue-equivalent material. *Radiology, 134*(2), 517-520. doi:10.1148/radiology.134.2.7352242

Carallo, C., Lucca, L. F., Ciamei, M., Tucci, S., & Franceschi, M. S. (2006). Wall shear stress is lower in the carotid artery responsible for a unilateral ischemic stroke. *Atherosclerosis, 185*(1), 108-113. doi:10.1016/j.atherosclerosis.2005.05.019

Carvalho, J. L., Nielsen, J., & Nayak, K. S. (2010). Feasibility of in vivo measurement of carotid wall shear rate using spiral fourier velocity encoded MRI. *Magnetic Resonance in Medicine, 63*(6), 1537-1547. doi:10.1002/mrm.22325

Cho, K. I., Kim, B. H., Kim, H. S., & Heo, J. H. (2016). Low Carotid Artery Wall Shear Stress is Associated with Significant Coronary Artery Disease in Patients with Chest Pain. *Journal of Atherosclerosis and Thrombosis, 23*(3), 297-308. doi:10.5551/jat.31377

Cobbold, R. S. (2007). *Foundations of biomedical ultrasound*. Oxford: Oxford University Press.

Craven, P., & Wahba, G. (1978). Smoothing noisy data with spline functions. *Numerische Mathematik, 31*(4), 377-403. doi:10.1007/bf01404567

Currie, I. G. (2013). *Fundamental mechanics of fluids*. Boca Raton: CRC Press.

Dhawan, S. S., Nanjundappa, R. P., Branch, J. R., Taylor, W. R., Quyyumi, A. A., Jo, H., . . . Samady, H. (2010). Shear stress and plaque development. *Expert Review of Cardiovascular Therapy, 8*(4), 545-556. doi:10.1586/erc.10.28

Daigle, R. E., & Kaczdowski, P. J. (2009). High frame rate quantitative Doppler flow imaging using unfocused transmit beams. *U.S. Patent Application No. 12/490,780*.

Donnan, G. A., Fisher, M., Macleod, M., & Davis, S. M. (2008). Stroke. *The Lancet, 371*(9624), 1612-1623. doi:10.1016/s0140-6736(08)60694-7

Duboeuf, F., Basarab, A., Liebgott, H., Brusseau, E., Delachartre, P., & Vray, D. (2009). Investigation of PVA cryogel Youngs modulus stability with time, controlled by a simple reliable technique. *Medical Physics, 36*(2), 656-661. doi:10.1118/1.3065031

Dunmire, B., Beach, K., Labs, K., Plett, M., & Strandness, D. (2000). Cross-beam vector Doppler ultrasound for angle-independent velocity measurements. *Ultrasound in Medicine & Biology, 26*(8), 1213-1235. doi:10.1016/s0301-5629(00)00287-8

Evans, D. H. (2010). Colour flow and motion imaging. *Proceedings of the Institution of Mechanical Engineers, Part H: Journal of Engineering in Medicine, 224*(2), 241-253. doi:10.1243/09544119jeim599

Evans, D. H., & McDicken, W. N. (2000). *Doppler ultrasound: Physics, instrumentation, and signal processing*. Chichester: Wiley.

Flaherty, J. J., Erikson, K. R., Lund, V. M. (1970). Synthetic aperture ultrasonic imaging systems. *U. S. Patent 3548642*. Washington, DC: U.S. Patent and Trademark Office.

Gaitini, D., & Soudack, M. (2005). Diagnosing Carotid Stenosis by Doppler Sonography. *Journal of Ultrasound in Medicine, 24*(8), 1127-1136. doi:10.7863/jum.2005.24.8.1127

Garcia, D. (2010). Robust smoothing of gridded data in one and higher dimensions with missing values. *Computational Statistics & Data Analysis, 54*(4), 1167-1178. doi:10.1016/j.csda.2009.09.020

Garcia, D. (2011). A fast all-in-one method for automated post-processing of PIV data. *Experiments in Fluids, 50*(5), 1247-1259. doi:10.1007/s00348-010-0985-y

Gemignani, V., Paterni, M., Benassi, A., & Demi, M. (2004). Real time contour tracking with a new edge detector. *Real-Time Imaging, 10*(2), 103-116. doi:10.1016/j.rti.2004.02.005

Gibson, C. M., Diaz, L., Kandarpa, K., Sacks, F. M., Pasternak, R. C., Sandor, T., . . . Stone, P. H. (1993). Relation of vessel wall shear stress to atherosclerosis progression in human coronary arteries. *Arteriosclerosis, Thrombosis, and Vascular Biology, 13*(2), 310-315. doi:10.1161/01.atv.13.2.310

Golemati, S., Sassano, A., Lever, M., Bharath, A. A., Dhanjil, S., & Nicolaides, A. N. (2003). Carotid artery wall motion estimated from b-mode ultrasound using region tracking and block matching. *Ultrasound in Medicine & Biology, 29*(3), 387-399. doi:10.1016/s0301-5629(02)00760-3

Gnasso, A., Irace, C., Carallo, C., Franceschi, M. S., Motti, C., Mattioli, P. L., & Pujia, A. (1997). In Vivo Association Between Low Wall Shear Stress and Plaque in Subjects With Asymmetrical Carotid Atherosclerosis. *Stroke, 28*(5), 993-998. doi:10.1161/01.str.28.5.993

Groen, H. C., Gijsen, F. J., Lugt, A. V., Ferguson, M. S., Hatsukami, T. S., Yuan, C., . . . Wentzel, J. J. (2008). High shear stress influences plaque vulnerability. *Netherlands Heart Journal, 16*(8), 280-283. doi:10.1007/bf03086163

Hansen, K., Udesen, J., Oddershede, N., Henze, L., Thomsen, C., Jensen, J., & Nielsen, M. (2009). In vivo comparison of three ultrasound vector velocity techniques to MR phase contrast angiography. *Ultrasonics, 49*(8), 659-667. doi:10.1016/j.ultras.2009.04.002

Hansen, P.L., Cross, G., Light, L.H. Beam-angle independent Doppler velocity measurement in superficial vessels. in: J.P. Woodcock (Ed.) Clinical blood flow measurement. Sector Publishing, London; 1974:28–32.

Hansen, F., Mangell, P., Sonesson, B., & Länne, T. (1995). Diameter and compliance in the human common carotid artery — variations with age and sex. *Ultrasound in Medicine & Biology, 21*(1), 1-9. doi:10.1016/0301-5629(94)00090-5

Haralick, R. M., & Shapiro, L. G. (1992). *Computer and robot vision* (Vol. I). Boston, USA: Addison-Wesley.

Hasegawa, H., & Kanai, H. (2008). Simultaneous imaging of artery-wall strain and blood flow by high frame rate acquisition of RF signals. *IEEE Transactions on Ultrasonics, Ferroelectrics, and Frequency Control*, *55*(12), 2626-2639.

Heart and Stroke Foundation of Canada, 'Statistics', 2016. [Online] Available: http://www.heartandstroke.com/site/c.ikIQLcMWJtE/b.3483991/k.34A8/Statistics.htm.

Herzog, C. A. (2008). Incidence of adverse events associated with use of Perflutren Contrast Agents for Echocardiography. *Jama, 299*(17), 2023. doi:10.1001/jama.299.17.2023

Ho, C. K., Chee, A. J., Yiu, B. Y., Tsang, A. C., Chow, K. W., & Yu, A. C. (2017). Wall-Less Flow Phantoms with Tortuous Vascular Geometries: Design Principles and a Patient-Specific Model Fabrication Example. *IEEE Transactions on Ultrasonics, Ferroelectrics, and Frequency Control, 64*(1), 25-38. doi:10.1109/tuffc.2016.2636129

Hobson, R. W., Wilson, S. E., & Veith, F. J. (2005). *Vascular surgery: Principles and practice*. London: Taylor & Francis.

Holfort, I., Gran, F., & Jensen, J. (2009). Broadband minimum variance beamforming for ultrasound imaging. *IEEE Transactions on Ultrasonics, Ferroelectrics and Frequency Control, 56*(2), 314-325. doi:10.1109/tuffc.2009.1040

Horikoshi, T., Akiyama, I., Yamagata, Z., Sugita, M., & Nukui, H. (2002). Magnetic resonance angiographic evidence of sex-linked variations in the circle of Willis and the occurrence of cerebral aneurysms. *Journal of Neurosurgery*, *96*(4), 697-703. doi:10.3171/jns.2002.96.4.0697

Hoskins, P. R. (2008). Simulation and Validation of Arterial Ultrasound Imaging and Blood Flow. *Ultrasound in Medicine & Biology*, *34*(5), 693-717. doi:10.1016/j.ultrasmedbio.2007.10.017

Hoskins, P. R. (2010). Haemodynamics and blood flow measured using ultrasound imaging. *Proceedings of the Institution of Mechanical Engineers, Part H: Journal of Engineering in Medicine, 224*(2), 255-271. doi:10.1243/09544119jeim572

Ingebrigtsen, T., Morgan, M. K., Faulder, K., Ingebrigtsen, L., Sparr, T., & Schirmer, H. (2004). Bifurcation geometry and the presence of cerebral artery aneurysms. *Journal of Neurosurgery*, *101*(1), 108-113. doi:10.3171/jns.2004.101.1.0108

Jensen, J. A., Nikolov, S. I., Gammelmark, K. L., & Pedersen, M. H. (2006). Synthetic aperture ultrasound imaging. *Ultrasonics, 44*. doi:10.1016/j.ultras.2006.07.017

Jensen, J. A., Nikolov, S. I., Yu, A. C., & Garcia, D. (2016). Ultrasound Vector Flow Imaging—Part II: Parallel Systems. *IEEE Transactions on Ultrasonics, Ferroelectrics, and Frequency Control, 63*(11), 1722-1732. doi:10.1109/tuffc.2016.2598180

Jin, S., Yang, Y., Oshinski, J., Tannenbaum, A., Gruden, J., & Giddens, D. (2004). Flow Patterns and Wall Shear Stress Distributions at Atherosclerotic-Prone Sites in a Human Left Coronary

Artery - An Exploration Using Combined Methods of CT and Computational Fluid Dynamics. *The 26th Annual International Conference of the IEEE Engineering in Medicine and Biology Society, 5*, 3789-91. doi:10.1109/iembs.2004.1404062

Johnson, B. F., Verlato, F., Bergelin, R. O., Primozich, J. F., & Strandness, D. (1995). Clinical outcome in patients with mild and moderate carotid artery stenosis. *Journal of Vascular Surgery, 21*(1), 120-126. doi:10.1016/s0741-5214(95)70250-4

Kasai, C., & Namekawa, K. (1985). Real-Time Two-Dimensional Blood Flow Imaging Using an Autocorrelation Technique. *IEEE 1985 Ultrasonics Symposium*. doi:10.1109/ultsym.1985.198654

Kefayati, S., & Poepping, T. L. (2013). Transitional flow analysis in the carotid artery bifurcation by proper orthogonal decomposition and particle image velocimetry. *Medical Engineering & Physics, 35*(7), 898-909. doi:10.1016/j.medengphy.2012.08.020

Kefayati, S., Milner, J. S., Holdsworth, D. W., & Poepping, T. L. (2014). In Vitro Shear Stress Measurements Using Particle Image Velocimetry in a Family of Carotid Artery Models: Effect of Stenosis Severity, Plaque Eccentricity, and Ulceration. *PLoS ONE, 9*(7). doi:10.1371/journal.pone.0098209

Kim, H., Hertzberg, J., Lanning, C., & Shandas, R. (2004). Noninvasive Measurement of Steady and Pulsating Velocity Profiles and Shear Rates in Arteries Using Echo PIV: In Vitro Validation Studies. *Annals of Biomedical Engineering, 32*(8), 1067-1076. doi:10.1114/b:abme.0000036643.45452.6d

Kinlay, S., Libby, P., & Ganz, P. (2001). Endothelial function and coronary artery disease. *Current Opinion in Lipidology, 12*(4), 383-389. doi:10.1097/00041433-200108000-00003

Koller, A., & Kaley, G. (1995). Endothelial Control of Shear Stress and Resistance in the Skeletal Muscle Microcirculation. *Flow-Dependent Regulation of Vascular Function*, 236-260. doi:10.1007/978-1-4614-7527-9_11

Kornet, L., Lambregts, J., Hoeks, A. P., & Reneman, R. S. (1998). Differences in Near-Wall Shear Rate in the Carotid Artery Within Subjects Are Associated with Different Intima-Media Thicknesses. *Arteriosclerosis, Thrombosis, and Vascular Biology, 18*(12), 1877-1884. doi:10.1161/01.atv.18.12.1877

Kortbek, J., Jensen, J. A., & Gammelmark, K. L. (2013). Sequential beamforming for synthetic aperture imaging. *Ultrasonics, 53*(1), 1-16. doi:10.1016/j.ultras.2012.06.006

Koskinas, K. C., Chatzizisis, Y. S., Baker, A. B., Edelman, E. R., Stone, P. H., & Feldman, C. L. (2009). The role of low endothelial shear stress in the conversion of atherosclerotic lesions from stable to unstable plaque. *Current Opinion in Cardiology, 24*(6), 580-590. doi:10.1097/hco.0b013e328331630b

Krejza, J., Arkuszewski, M., Kasner, S. E., Weigele, J., Ustymowicz, A., Hurst, R. W., . . . Messe, S. R. (2006). Carotid Artery Diameter in Men and Women and the Relation to Body and Neck Size. *Stroke, 37*(4), 1103-1105. doi:10.1161/01.str.0000206440.48756.f7

Ku, D. N., Giddens, D. P., Zarins, C. K., Glagov, S. (1985) Pulsatile flow and atherosclerosis in the human carotid bifurcation. Positive correlation between plaque location and low oscillating shear stress. *Arteriosclerosis*, *5*(3), 293-302.

Lankton, S., & Tannenbaum, A. (2008). Localizing Region-Based Active Contours. *IEEE Transactions on Image Processing, 17*(11), 2029-2039. doi:10.1109/tip.2008.2004611

Lauric, A., Hippelheuser, J., Safain, M. G., & Malek, A. M. (2014). Curvature effect on hemodynamic conditions at the inner bend of the carotid siphon and its relation to aneurysm formation. *Journal of Biomechanics, 47*(12), 3018-3027. doi:10.1016/j.jbiomech.2014.06.042

Leow, C. H., Bazigou, E., Eckersley, R. J., Yu, A. C., Weinberg, P. D., & Tang, M. (2015). Flow Velocity Mapping Using Contrast Enhanced High-Frame-Rate Plane Wave Ultrasound and Image Tracking: Methods and Initial in Vitro and in Vivo Evaluation. *Ultrasound in Medicine & Biology, 41*(11), 2913-2925. doi:10.1016/j.ultrasmedbio.2015.06.012

Leow, C. H., & Tang, M. (2018). Spatio-Temporal Flow and Wall Shear Stress Mapping Based on Incoherent Ensemble-Correlation of Ultrafast Contrast Enhanced Ultrasound Images. *Ultrasound in Medicine & Biology*, *44*(1), 134-152. doi:10.1016/j.ultrasmedbio.2017.08.930

Madsen, E. L., Zagzebski, J. A., & Frank, G. R. (1982). Oil-in-gelatin dispersions for use as ultrasonically tissue-mimicking materials. *Ultrasound in Medicine & Biology, 8*(3), 277-287. doi:10.1016/0301-5629(82)90034-5

Makris, G. C., Nicolaides, A. N., Xu, X. Y., & Geroulakos, G. (2010). Introduction to the biomechanics of carotid plaque pathogenesis and rupture: Review of the clinical evidence. *The British Journal of Radiology, 83*(993), 729-735. doi:10.1259/bjr/49957752

Malek, A. M., Alper S. L., Izumo, S. (1999). Hemodynamic Shear Stress and Its Role in Atherosclerosis. *Jama, 282*(21), 2035. doi:10.1001/jama.282.21.2035

Martin, D., Zaman, A., Hacker, J., Mendelow, D., & Birchall, D. (2009). Analysis of haemodynamic factors involved in carotid atherosclerosis using computational fluid dynamics. *The British Journal of Radiology, 82*(Special_issue_1). doi:10.1259/bjr/59367266

Mehta, K. S., Lee, J. J., Taha, A. A., Avgerinos, E., & Chaer, R. A. (2017). Vascular applications of contrast-enhanced ultrasound imaging. *Journal of Vascular Surgery, 66*(1), 266-274. doi:10.1016/j.jvs.2016.12.133

Mo, L., Ji, T., Chou, C., Napolitano, D., Mclaughlin, G., & Debusschere, D. (n.d.). Zone-based color flow imaging. *IEEE Symposium on Ultrasonics, 2003*. doi:10.1109/ultsym.2003.1293350

Montaldo, G., Tanter, M., Bercoff, J., Benech, N., & Fink, M. (2009). Coherent plane-wave compounding for very high frame rate ultrasonography and transient elastography. *IEEE Transactions on Ultrasonics, Ferroelectrics and Frequency Control, 56*(3), 489-506. doi:10.1109/tuffc.2009.1067

Moore, C. L., & Copel, J. A. (2011). Point-of-Care Ultrasonography. *New England Journal of Medicine, 364*(8), 749-757. doi:10.1056/nejmra0909487

Morris, P. D., Narracott, A., Tengg-Kobligk, H. V., Soto, D. A., Hsiao, S., Lungu, A., . . . Gunn, J. P. (2015). Computational fluid dynamics modelling in cardiovascular medicine. *Heart, 102*(1), 18-28. doi:10.1136/heartjnl-2015-308044

Murphy, E. A., Ross, R. A., Jones, R. G., Gandy, S. J., Aristokleous, N., Salsano, M., . . . Houston, J. G. (2017). Imaging in Vascular Access. *Cardiovascular Engineering and Technology, 8*(3), 255-272. doi:10.1007/s13239-017-0317-y

Mynard, J. P., Wasserman, B. A., & Steinman, D. A. (2013). Errors in the estimation of wall shear stress by maximum Doppler velocity. *Atherosclerosis, 227*(2), 259-266. doi:10.1016/j.atherosclerosis.2013.01.026

Nayer, A., & Ortega, L. M. (2014). Catastrophic antiphospholipid syndrome: a clinical review. *Journal of Nephropathology, 3*(1), 9-17. doi:10.12860/jnp.2014.03

Nixon, A. M., Gunel, M., & Sumpio, B. E. (2010). The critical role of hemodynamics in the development of cerebral vascular disease. *Journal of Neurosurgery, 112*(6), 1240-1253. doi:10.3171/2009.10.jns09759

Oshinski, J. N., Curtin, J. L., Loth, F. (2006). Mean-average wall shear stress measurements in the common carotid artery. *Journal of Cardiovascular Magnetic Resonance, 8*(5), 717-722.

Owen, D. R., Lindsay, A. C., Choudhury, R. P., Fayad, Z. A. (2011). Imaging of atherosclerosis. *Annual Review of Medicine, 62*,25-40. doi: 10.1146/annurev-med-041709-133809.

Peronneau, P., Bournat, J. P., Bugnon, A., Barbet. A., Xhaard, M. (1974). Theoretical and practical aspects of pulsed Doppler flowmetry: Realtime application to the measure of instantaneous velocity profiles *in vitro* and *in vivo*. In: Reneman, R., S. (Ed). *Cardiovascular Applications of Ultrasound*. 866-884. Amsterdam, The Netherlands: North Holland

Poepping, T. L., Rankin, R. N., & Holdsworth, D. W. (2010). Flow Patterns in Carotid Bifurcation Models Using Pulsed Doppler Ultrasound: Effect of Concentric vs. Eccentric Stenosis on Turbulence and Recirculation. *Ultrasound in Medicine & Biology, 36*(7), 1125-1134. doi:10.1016/j.ultrasmedbio.2010.02.005

Ramnarine, K. V., Nassiri, D. K., Hoskins, P. R., & Lubbers, J. (1998). Validation of a New Blood-Mimicking Fluid for Use in Doppler Flow Test Objects. *Ultrasound in Medicine & Biology, 24*(3), 451-459. doi:10.1016/s0301-5629(97)00277-9

Ramnarine, K. V., Anderson, T., & Hoskins, P. R. (2001). Construction and geometric stability of physiological flow rate wall-less stenosis phantoms. *Ultrasound in Medicine & Biology, 27*(2), 245-250. doi:10.1016/s0301-5629(00)00304-5

Reneman, R. S., Arts, T., Hoeks, A. P. (2006). Wall shear stress--An important determinant of endothelial cell function and structure—In the arterial system in vivo. Discrepancies with theory. *Journal of Vascular Research, 43(3),*251-269

Reneman, R. S., Woldhuis, B., Egbrink, M. G., Slaaf, D. W., & Tangelder, G. J. (1992). Concentration and Velocity Profiles of Blood Cells in the Microcirculation. *Advances in Cardiovascular Engineering*, 25-40. doi:10.1007/978-1-4757-4421-7_3

Resnick, N., Yahav, H., Shay-Salit, A., Shushy, M., Schubert, S., Zilberman, L. C., & Wofovitz, E. (2003). Fluid shear stress and the vascular endothelium: For better and for worse. *Progress in Biophysics and Molecular Biology, 81*(3), 177-199. doi:10.1016/s0079-6107(02)00052-4

Ricci, S., Swillens, A., Ramalli, A., Segers, P., & Tortoli, P. (2017). Wall Shear Rate Measurement: Validation of a New Method Through Multiphysics Simulations. *IEEE Transactions on Ultrasonics, Ferroelectrics, and Frequency Control, 64*(1), 66-77. doi:10.1109/tuffc.2016.2608442

Roark, R. J., Young, W. C., & Budynas, R. G. (2002). *Roark's formulas for stress and strain*. New York: McGraw-Hill.

Sandrin, L., Manneville, S., & Fink, M. (2001). Ultrafast two-dimensional ultrasonic speckle velocimetry: A tool in flow imaging. *Applied Physics Letters, 78*(8), 1155-1157. doi:10.1063/1.1350622

Shields, R. C. (2010). Medical Management of Carotid Stenosis. *Perspectives in Vascular Surgery and Endovascular Therapy, 22*(1), 18-27. doi:10.1177/1531003510380929

Smith, R. F., Rutt, B. K., Fox, A. J., & Rankin, R. N. (1996). Geometric characterization of stenosed human carotid arteries. *Academic Radiology, 3*(11), 898-911. doi:10.1016/s1076-6332(96)80297-2

Smith, R. F., Rutt, B. K., & Holdsworth, D. W. (1999). Anthropomorphic carotid bifurcation phantom for MRI applications. *Journal of Magnetic Resonance Imaging, 10*(4), 533-544. doi:10.1002/(sici)1522-2586(199910)10:43.3.co;2-q

So, H., Chen, J., Yiu, B., & Yu, A. (2011). Medical Ultrasound Imaging: To GPU or Not to GPU? *IEEE Micro, 31*(5), 54-65. doi:10.1109/mm.2011.65

Sobel, I., & Feldman, G. (1968). A 3×3 Isotropic Gradient Operator for Image Processing. A Talk at the Stanford Artificial Project, 271-272.

Spence, J. D. (2013). Asymptomatic Carotid Stenosis. *Circulation, 127*(6), 739-742. doi:10.1161/circulationaha.112.153734

Spence, J. D., & Naylor, A. R. (2016). Endarterectomy, Stenting, or Neither for Asymptomatic Carotid-Artery Stenosis. *New England Journal of Medicine, 374*(11), 1087-1088. doi:10.1056/nejme1600123

Stauffer, S. R., & Peppast, N. A. (1992). Poly(vinyl alcohol) hydrogels prepared by freezing-thawing cyclic processing. *Polymer, 33*(18), 3932-3936. doi:10.1016/0032-3861(92)90385-a

Stride, E. P., & Coussios, C. C. (2010). Cavitation and contrast: The use of bubbles in ultrasound imaging and therapy. *Proceedings of the Institution of Mechanical Engineers, Part H: Journal of Engineering in Medicine, 224*(2), 171-191. doi:10.1243/09544119jeim622

Struijk, P., Stewart, P., Fernando, K., Mathews, V., Loupas, T., Steegers, E., & Wladimiroff, J. (2005). Wall shear stress and related hemodynamic parameters in the fetal descending aorta derived from color Doppler velocity profiles. *Ultrasound in Medicine & Biology, 31*(11), 1441-1450. doi:10.1016/j.ultrasmedbio.2005.07.006

Surry, K. J., Austin, H. J., Fenster, A., & Peters, T. M. (2004). Poly(vinyl alcohol) cryogel phantoms for use in ultrasound and MR imaging. *Physics in Medicine and Biology, 49*(24), 5529-5546. doi:10.1088/0031-9155/49/24/009

Swillens, A., Segers, P., Torp, H., & Lovstakken, L. (2010). Two-dimensional blood velocity estimation with ultrasound: Speckle tracking versus crossed-beam vector doppler based on flow simulations in a carotid bifurcation model. *IEEE Transactions on Ultrasonics, Ferroelectrics and Frequency Control, 57*(2), 327-339. doi:10.1109/tuffc.2010.1413

Tangelder, G. J., Slaaf, D. W., Muijtjens, A. M., Arts, T., Egbrink, M. G., & Reneman, R. S. (1986). Velocity profiles of blood platelets and red blood cells flowing in arterioles of the rabbit mesentery. *Circulation Research, 59*(5), 505-514. doi:10.1161/01.res.59.5.505

Tanter, M., & Fink, M. (2014). Ultrafast imaging in biomedical ultrasound. *IEEE Transactions on Ultrasonics, Ferroelectrics, and Frequency Control, 61*(1), 102-119. doi:10.1109/tuffc.2014.2882

Tsou, J. K., Liu, J., Barakat, A. I., & Insana, M. F. (2008). Role of Ultrasonic Shear Rate Estimation Errors in Assessing Inflammatory Response and Vascular Risk. *Ultrasound in Medicine & Biology, 34*(6), 963-972. doi:10.1016/j.ultrasmedbio.2007.11.010

Tuenter, A., Selwaness, M., Lorza, A. A., Schuurbiers, J., Speelman, L., Cibis, M., . . . Wentzel, J. (2016). High shear stress relates to intraplaque haemorrhage in asymptomatic carotid plaques. *Atherosclerosis, 251*, 348-354. doi:10.1016/j.atherosclerosis.2016.05.018

Usami, S., Chen, H., Zhao, Y., Chien, S., & Skalak, R. (1993). Design and construction of a linear shear stress flow chamber. *Annals of Biomedical Engineering, 21*(1), 77-83. doi:10.1007/bf02368167

Wahba, G. (1990). *Spline models for observational data*. Philadelphia: Society for Industrial and Applied Mathematics.

Wang, W. Q., Yao, L. X. (1982). A double beam doppler ultrasound method for quantitative blood flow velocity measurement. *Ultrasound in Medicine & Biology, 8*(4), 421-425. doi:10.1016/s0301-5629(82)80010-0

Weaver, J. (2013). Insights into How Calcium Forms Plaques in Arteries Pave the Way for New Treatments for Heart Disease. *PLoS Biology, 11*(4). doi:10.1371/journal.pbio.1001533

Weber, C., & Noels, H. (2011). Atherosclerosis: Current pathogenesis and therapeutic options. *Nature Medicine, 17*(11), 1410-1422. doi:10.1038/nm.2538

Weinert, H. L. (2007). Efficient computation for Whittaker–Henderson smoothing. *Computational Statistics & Data Analysis, 52*(2), 959-974. doi:10.1016/j.csda.2006.11.038

Whittaker, E. (1923). On a New Method of Graduation. *Proceedings of the Edinburgh Mathematical Society, 41*, 63-75. doi:10.1017/S0013091500077853

Womersley, J. R. (1955). Method for the calculation of velocity, rate of flow and viscous drag in arteries when the pressure gradient is known. *The Journal of Physiology, 127*(3), 553-563. doi:10.1113/jphysiol.1955.sp005276

Wong, E. Y., Nikolov, H. N., Thorne, M. L., Poepping, T. L., Rankin, R. N., & Holdsworth, D. W. (2009). Clinical Doppler ultrasound for the assessment of plaque ulceration in the stenosed carotid bifurcation by detection of distal turbulence intensity: A matched model study. *European Radiology, 19*(11), 2739-2749. doi:10.1007/s00330-009-1457-8

World Health Organization. (2017). Cardiovascular diseases [Fact Sheet]. Retrieved March 28, 2018, from http://www.who.int/mediacentre/factsheets/fs317/en/

Xu, C., Choi, J. H., Comess, K., & Kim, Y. (2010). Color Doppler and spectral Doppler with high frame-rate imaging. *2010 IEEE International Ultrasonics Symposium*. doi:10.1109/ultsym.2010.5935670

Yim, P., Demarco. K., Castro, M. A. (2005). Characterization of shear stress on the wall of the carotid artery using magnetic resonance imaging and computational fluid dynamics. *Studies in Health Technology and Informatics, 113,412*-442

Yiu, B. Y., Lai, S. S., & Yu, A. C. (2014). Vector Projectile Imaging: Time-Resolved Dynamic Visualization of Complex Flow Patterns. *Ultrasound in Medicine & Biology, 40*(9), 2295-2309. doi:10.1016/j.ultrasmedbio.2014.03.014

Yiu, B. Y., Tsang, I. K., & Yu, A. C. (2011). GPU-based beamformer: Fast realization of plane wave compounding and synthetic aperture imaging. *IEEE Transactions on Ultrasonics, Ferroelectrics and Frequency Control, 58*(8), 1698-1705. doi:10.1109/tuffc.2011.1999

Yiu, B. Y., & Yu, A. C. (2013). High-Frame-Rate Ultrasound Color-Encoded Speckle Imaging of Complex Flow Dynamics. *Ultrasound in Medicine & Biology, 39*(6), 1015-1025. doi:10.1016/j.ultrasmedbio.2012.12.016

Yiu, B. Y., & Yu, A. C. (2016). Least-Squares Multi-Angle Doppler Estimators for Plane-Wave Vector Flow Imaging. *IEEE Transactions on Ultrasonics, Ferroelectrics, and Frequency Control, 63*(11), 1733-1744. doi:10.1109/tuffc.2016.2582514

Zhang, F., Lanning, C., Mazzaro, L., Barker, A. J., Gates, P. E., Strain, W. D., . . . Shandas, R. (2011). In Vitro and Preliminary In Vivo Validation of Echo Particle Image Velocimetry in Carotid Vascular Imaging. *Ultrasound in Medicine & Biology, 37*(3), 450-464. doi:10.1016/j.ultrasmedbio.2010.11.017

# Appendix A

This appendix is a video of the spatiotemporal WSR profile inside a healthy carotid bifurcation phantom.

The file name of this video is “Movie 1 WSR in healthy model.mp4”.

# Appendix B

This appendix is a video of the spatiotemporal WSR profile inside a 50% stenosed carotid bifurcation phantom.

The file name of this video is “Movie 2 WSR in diseased model.mp4”.